

# Bachelor Thesis

## Finding an Optimal Regularisation Parameter for the Inversion of Transient Electromagnetic Data Using the L-Curve Method

Peter Balogh

e12202337@student.tuwien.ac.at

Matr.Nr. 1220 2337

Date: November 19, 2025

Supervisor: Associate Prof. Dr.rer.nat. Adrian Flores-Orozco

### Abstract

## 1 Introduction

## 2 Materials and Methods

The TEM method was originally introduced for mining applications (Chandra 2016) and was since adopted to other fields like groundwater, and geothermal exploration (Chandra 2016; Everett 2013). The transient electromagnetic (TEM) or alternatively time-domain electromagnetic (TDEM) method was proposed by Obukhov (1968) and has been intensively developed in the 1980s (Christiansen et al. 2006).

### 2.1 Transient Electromagnetic Method

For the TEM method a pulse of current is transmitted through a ungrounded transmitter loop generating a primary magnetic field (Chandra 2016; Christiansen et al. 2006). When the current is turned off, the decay of the primary field induces secondary currents (eddy currents) in the ground, which produce a secondary magnetic field (Chandra 2016; Christiansen et al. 2006). This is governed by the Maxwell equations, which state that a changing electrical field

induces a magnetic field, and vice versa (Christiansen et al. 2006). An electromagnetic (EM) wave propagating through the subsurface, is attenuated by the electrical properties of the materials it encounters (Christiansen et al. 2006; Everett 2013). The strength of the secondary magnetic field depends on the conductivity of the material the EM wave propagates through and by measuring this field over time using a receiver loop, information about the subsurface can be obtained (Christiansen et al. 2006; Chandra 2016). Data is recorded in specific time-windows (gates), which are usually logarithmically spaced to increase signal-to-noise (S/N) ratio in later times, which is called logging (Christiansen et al. 2006). Such a decay curve of the secondary magnetic field over time is called a “transient”, with an numerically modelled example shown in Figure 1(b).

By analysing the decay characteristics of a transient, it is possible to infer the conductivity structure of the subsurface, because with passing time the EM wave propagates deeper into the subsurface and thus later time gates are linked to information about deeper layers (Christiansen et al. 2006). The depth of investigation

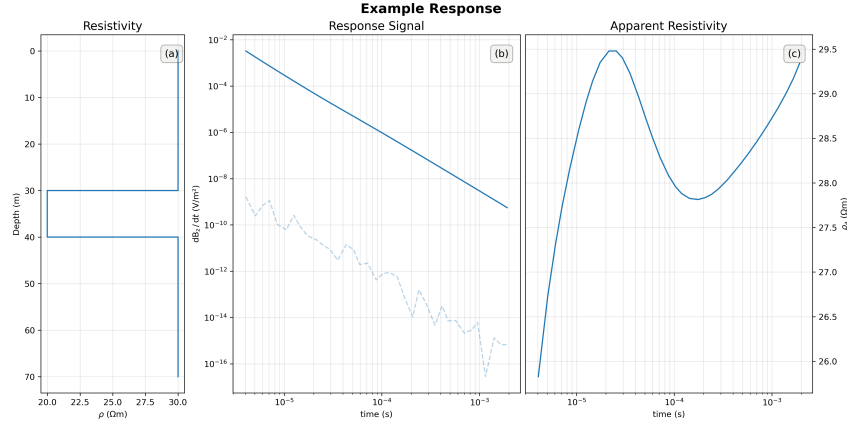


**Fig. 1:** Numerically modelled typical TEM response with the used subsurface model (a), the signal (b), and the apparent resistivity (c).

(DOI) is limited by the electrical conductivity of the subsurface, because a EM wave attenuates stronger within a conductive layer (Everett 2013). For this reason the TEM method is commonly deployed to investigate conductive layers such as sea water intrusions, and clay layers confining aquifers (Chandra 2016).

Every geophysical measurement includes uncertainty and a single transient is usually significantly influenced by background noise (Christiansen et al. 2006; Everett 2013). To increase the S/N ratio of a TEM sounding measurements are repeated and the resulting transients are combined, which is called “stacking” (Christiansen et al. 2006). Commonly between 1000 and 10000 transients are stacked into one sounding (Aigner et al. 2021) and when utilising a log-gating technique the S/N ratio is improved by the factor  $\sqrt{N}$  where  $N$  is the amount of measurements per stack (Christiansen et al. 2006).

A first evaluation of the data collected can be to convert the transient from voltage readings to apparent electrical resistivity ( $\rho_a$ ), which equals to the weighted mean of the resistivities of the layers in which the currents were induced (Siemon 2009). If the EM wave travels through a half-space, the late-time apparent resistivities is given by

$$\rho_a = \frac{1}{\pi} \left( \frac{M}{20 \cdot \frac{\partial b_z}{\partial t}} \right)^{\frac{2}{3}} \left( \frac{\mu_0}{t} \right)^{\frac{5}{3}} \quad (1)$$

where  $M$  is the magnetic moment,  $\frac{\partial b_z}{\partial t}$  is the signal measured by the receiver coil,  $\mu_0$  is the magnetic permeability of free space and  $t$  is

the time (Fitterman et al. 1986). The magnetic moment is the product of the number of turns, the area, and the current in the transmitter loop. Figure 1 shows a numerically modelled example, where (a) is the one dimensional model of the layered half-space, (b) is the modelled decay of the secondary magnetic field, and (c) shows the converted apparent resistivity. Figure 1 shows that in a layered half-space the resistivities of the subsurface model in (a) can not be simply inferred through the apparent resistivities in (c), which makes the interpretation of the data necessary (Fitterman et al. 1986; Christiansen et al. 2006). Reconstructing the resistivity distribution of the subsurface requires the solution of ill-posed problem, as there are many subsurface models, which can explain the measured data (Xue et al. 2020). Inferring a subsurface model from observed data is called an inverse problem or “inversion” and will be discussed in Section 2.2.3. For the interpretation of TEM data – and for the inversion in particular – the following assumptions must to be made: The EM waves created by the transmitter only propagate downwards into a layered half-space and as most inversion algorithms work with a one dimensional model, the subsurface is assumed to be homogeneous in the horizontal direction (Christiansen et al. 2006).

## 2.2 State of The Art

Even with these limitations the TEM method has found widespread application in environmental applications like groundwater explo-

ration (Danielsen et al. 2003; Sorensen et al. 2004; Auken et al. 2019), delineating saline intrusions into the groundwater (Gómez et al. 2019; Gonzales Amaya et al. 2018), characterising the subsurface below continental water bodies (Aigner et al. 2021), and the detection of karstic features (Zhou et al. 2022; Su et al. 2024).

### 2.2.1 Environmental Applications of TEM

Danielsen et al. (2003) used the TEM method for the exploration of buried valleys as potential aquifers in Denmark. The study introduced two new TEM systems based on the Geonics PROTEM: The high moment transient electromagnetic (HiTEM) system for a deeper investigation depth, and the pulled array Transient electromagnetic (PATEM) system for a higher lateral resolution. The HiTEM system uses a combination of a  $30 \times 30$  m transmitter loop and a current of 75 m to achieve a depth of investigation (DOI) of up to 300 m (Danielsen et al. 2003). To mitigate distortion effects a HiTEM sounding is split into two parts: A 70 m offset loop configuration for the later time data, and a central loop configuration with a reduced current of 2.5 A for the early times (Danielsen et al. 2003). A mutually constrained inversion (MCI) like in Auken et al. (2005) is used to invert the combination of the data gathered with the two different configurations (Danielsen et al. 2003). Danielsen et al. (2003) developed the PATEM system to use a  $3 \times 5$  m transmitter loop on a wheeled frame with an offset receiver loop, which allows for continuous measurements along a profile and a DOI of 100 – 150 m. To achieve a high DOI and useful near surface information, the PATEM system allows for a transmitter configuration with either 2 turns with 16 A or 8 turns with 40 – 50 A (Danielsen et al. 2003). That study also touches on the problems resulting from coupling with man-made structures. Coupling noise can be described as the noise introduced through induced currents in man-made structures, which changes the decay characteristics of the secondary magnetic field, and can be divided into galvanic and capacitive (Christiansen et al. 2006). Galvanic coupling is caused by grounded conductors like power lines and causes an underestimation of

the resistivity (Christiansen et al. 2006). Capacitive coupling is caused by current being generated in the conductor and leaking into the ground through an insulation, which leads to an oscillating signal (Christiansen et al. 2006). For this reason the Danielsen et al. (2003) recommend keeping a distance of about 150 m from underground cables or pipes when the earth has a resistivity of  $40 - 50 \Omega\text{m}$ .

Similarly to the PATEM system, Auken et al. (2019) propose a towed transient electromagnetic (tTEM) system for an efficient 3D mapping of the subsurface. The tTEM system utilises a  $2 \times 4$  m transmitter loop mounted on a non-conductive sled towed by a vehicle, which enables a production rate of about  $1 \text{ km}^2$  per day (Auken et al. 2019). The receiver loop is towed at 9 m offset from the transmitter (Auken et al. 2019). Like the PATEM system (Danielsen et al. 2003), the tTEM system (Auken et al. 2019) permits the use of two different currents (2.8 and 30 A) in order to gain a relatively high DOI of up to 70 m, while still allowing the investigation of shallow depths. Auken et al. (2019) also highlight the importance of considering the coupling effects of the system with conductive objects and it tests the system in an environment with a high resistivity of the subsurface ( $> 600 \Omega\text{m}$ ). Under these circumstances the signal caused by coupling can be observed in isolation and the study found that a minimal distance of 3 m between transmitter and vehicle was necessary to mitigate coupling effects (Auken et al. 2019).

Electromagnetic methods do not require direct contact with the subsurface, which allowed for the development of airborne electromagnetic methods (AEM) (Christiansen et al. 2006). Sorensen et al. (2004) introduced the SkyTEM system as an alternative to ground based TEM systems. The SkyTEM system uses a helicopter to carry a  $12.5 \times 12.5$  m transmitter loop with 4 turns and a receiver loop ( $0.5 \times 0.5$  m) in a central configuration (Sorensen et al. 2004). Just like the PATEM and HiTEM systems (Danielsen et al. 2003), a low moment and a high moment configuration are used to achieve a high DOI, while still resolving the near surface layers (Sorensen et al. 2004). In the low moment configuration the current of 35 A only flows through one turn and for the high mo-

ment 50 A are used with all 4 turns (Sorensen et al. 2004). Sorensen et al. (2004) validated the SkyTEM system against a ground based TEM system with a transmitter loop size of  $40 \times 40$  m, showing a good agreement (below 5% deviation). This system is able to cover a larger area than traditional ground based systems in the same amount of time, while still being able to resolve underground structures, such as buried valleys (Sorensen et al. 2004).

To investigate the subsurface below continental bodies of water, Aigner et al. (2021) propose a flexible single loop system which can be towed by a boat. This is made possible through the TEM-FAST Technology, which allows for one loop to function as the transmitter and receiver antenna (Barsukov et al. 2006). The single loop is kept afloat by several PVC pipe segments, that keep it in a circular shape, which allows the system to be moved around the lake with ease (Aigner et al. 2021). Using multiple pipe segments allows for different loop sizes and thus different investigation depths (Aigner et al. 2021). Aigner et al. (2021) used the TEM-FAST 48 system by Applied Electromagnetic Research (AEMR) to investigate the subsurface of the Lake Langau in Austria. A current of 4 A and loops with radii between  $6.2 - 11.9$  m were used, leading to an investigation depth between  $6.2 - 50.0$  m, which was sufficient to detect sedimentary layers below the lake (Aigner et al. 2021). Aigner et al. (2021) highlight the importance of understanding how long the turn-off time of the transmitter for a single-loop setup is, to be able to properly interpret early time data. When the transmitter is turned off, the current in the loop takes a certain amount of time to decay, which is called the “turn-off ramp” (Christiansen et al. 2006). As the transmitter and receiver antennae are the same loop, the turn-off ramp affect the early time readings, which Barsukov et al. (2006) also describes as the “self-transient process”. Visually the effects of the turn-off ramp can be seen as an increase of the apparent resistivity values in the early times independent from the structure of the electrical properties in the subsurface (Aigner et al. 2021). Aigner et al. (2021) measured the time, which turn-off ramp lasted, (minimum effective time) for the TEM-FAST 48 to be between  $4.2 - 10.4 \mu\text{s}$  – depending on loop size

and resistivity of the subsurface. Using this information, a formula was derived to find the minimum effective sounding depth:

$$h_{\text{eff}} = \sqrt{t_{\text{eff}} \bar{\rho}} \quad (2)$$

where  $h_{\text{eff}}$  is the minimum effective sounding depth,  $t_{\text{eff}}$  is the minimum effective time and  $\bar{\rho}$  is the average resistivity of the smooth subsurface model (Aigner et al. 2021).

The study by Aigner et al. (2021) also showcases two different approaches to finding the DOI. The first uses different starting models for the inversion assuming that the DOI is reached when the data does not influence the inverted model anymore and will keep the values of the starting model (Aigner et al. 2021). The second approach is based on the formula:

$$\text{DOI} \approx 0.55 \left( \frac{M \times \bar{\rho}}{\eta} \right) \quad (3)$$

where  $M$  is the magnetic moment,  $\bar{\rho}$  is the average resistivity of the smooth subsurface model and  $\eta$  is the noise level (Aigner et al. 2021). Both methods agree on a DOI ranging between 20 and 50 m depending on the loop size (Aigner et al. 2021).

Gonzales Amaya et al. (2018) show the potential of the TEM method for the exploration of groundwater in the Punata alluvial fan. This aquifer is an important water source for the region, but it has zones with high salinity, which poses challenges in its use (Gonzales Amaya et al. 2018). This study used the ABEM Walk-TEM system with a  $50 \times 50$  m transmitter loop with a current of 18 A and two receiver loops ( $0.5 \times 0.5$  m and  $10 \times 10$  m) in a central configuration (Gonzales Amaya et al. 2018). This way a DOI of up to 200 m was achieved in some regions of the alluvial fan, while in other regions the DOI was limited to 80 m (Gonzales Amaya et al. 2018). Gonzales Amaya et al. (2018) were able to detect zones with electrical resistivities of  $0.1 - 1 \Omega\text{m}$ , which indicate high salinity (brine layer). The results from the TEM soundings showed good agreement with borehole and electrical resistivity tomography (ERT) data and were even able to discern a potential fault in the bedrock not detected by the other methods (Gonzales Amaya et al. 2018).

Gómez et al. (2019) conducted a similar study in the Challapampa area, Bolivia. In this study the same WalkTEM system was used, yet the receiver loops were deployed in an offset configuration and for the  $0.5 \times 0.5$  m loop only a current of 2 A was used, while the whole 18 A were applied for the  $10 \times 10$  m loop (Gómez et al. 2019). This setup achieved a depth of investigation (DOI) of up to 250 m and identified the influence of a hot spring, which appeared as a low-resistivity zone ( $5 \Omega\text{m}$ ), indicating higher salinity (Gómez et al. 2019).

Another application of TEM is the detection of karstic features, like caves, faults, and fracture zones (Zhou et al. 2022; Su et al. 2024). Traditionally, a large transmitter loop size in the order of 100 m side length was used to achieve a high investigation depth, which made the TEM method not suitable for the application in mountainous regions (Zhou et al. 2022; Su et al. 2024). However, a similar investigation depth can be achieved by using a smaller transmitter loop size and more turns (Zhou et al. 2022). The disadvantage being that a multi-turn setup is affected by mutual inductance caused by the large number of turns, which can lead to underestimation of the resistivity of the subsurface (Zhou et al. 2022).

Zhou et al. (2022) propose a coincident configuration with a  $2 \times 2$  m loop size and 10 turns for the transmitter, and 20 turns for the receiver antenna using the TEM system “YCS512” by Fuzhou Huahong Intelligent Technology Co., Ltd., China. The authors of this study did not disclose the acquisition time used for the soundings, but Chengshuai et al. (2024) describe the YCS512 system to have a sampling time window of  $9500 \mu\text{s}$ . To mitigate the effects of the mutual inductance, borehole and ERT data were used to constrain the inversion (Zhou et al. 2022). As boreholes and ERT measurements are expensive and time-consuming, they were used at a single sounding location to quantify the shift in the resistivity values caused by mutual inductance, which was then used to correct the remaining TEM soundings (Zhou et al. 2022). Zhou et al. (2022) were able to discern an area with a electrical resistivity of  $80 \Omega\text{m}$  in the results obtained through the TEM measurements, which indicate a potential underground karst channel. The constrained inversion of the TEM data showed

consistent agreement with real strata, but the abnormal zones obtained through ERT and TEM showed minor discrepancies due to the different underlying principles of the two methods (Zhou et al. 2022).

A more in-depth study on how to deal with self and mutual inductance was conducted by Su et al. (2024). Here a central loop configuration (receiver loop in the centre of the transmitter loop) with a  $1.5 \times 1.5$  m transmitter loop and 6 turns was compared with a multi-turn small fixed-loop configuration (using multiple different receiver positions, while keeping the transmitter loop fixed) with a  $3 \times 3$  m transmitter loop and a single turn (Su et al. 2024). The ProTEM47HP system was used for both configurations with a current of 1.5 A and a turn-off time of  $5 - 25 \mu\text{s}$  (Su et al. 2024). For the fixed-loop set up a correction coefficient was introduced to account for off-centre receiver positions (Su et al. 2024). Su et al. (2024) conducted 5 model tests in a  $5 \times 4 \times 3$  m sand-filled area to compare the two configurations and the results showed that after correction the fixed-loop configuration was more accurate in detecting the position of one or multiple anomalies.

## 2.2.2 Common Electrical Resistivities of Subsurface Media

Electrical resistivity (or conductivity), seismic velocities, and dielectric constant are the most relevant petrophysical properties used in geophysical investigations to identify the geological composition of the subsurface (Kirsch 2006). The TEM method is mainly used to infer the electrical resistivity of the subsurface (Christiansen et al. 2006), although there are newer approaches to also characterise polarisation effects (Aigner et al. 2024). By analysing the electrical resistivity values, it is possible to infer the composition of subsurface layers and detect geological structures such as faults and fractures (Zhou et al. 2022; Su et al. 2024), and aquifers (Danielsen et al. 2003; Auken et al. 2019; Gonzales Amaya et al. 2018; Gómez et al. 2019). Table 1 presents commonly reported resistivity values for common geological media relevant to groundwater exploration.

These values have been compiled from multiple studies conducted in diverse geological

**Tab. 1:** Common Resistivity Values of Sub-surface Materials

Material	Resistivity ( $\Omega\text{m}$ )
Saturated layers with high salinity	0.1 – 5
Saturated clays and silts	5 – 15
Saturated sediments	10 – 20
Unsaturated sediments	50 – 80
Saturated sand	40 – 150
Unsaturated sand	400 – 1500

settings and using various geophysical methods (Gómez et al. 2019; Galazoulas et al. 2015; George et al. 2022). In the context of Table 1, the term “sediments” refers to unconsolidated deposits consisting of a mixture of sand, silt, and clay. The precise resistivity values presented in Table 1 for sediments are not general global values but are specific to the study region investigated by Gómez et al. (2019). These values reflect the characteristics of sediments found in the Challapampa aquifer in Bolivia, where variations in grain size, moisture content, and mineral composition influence the resistivity measurements.

### 2.2.3 Data Inversion

Zhdanov (2002) defines a typical geophysical problem can be defined as follows:

$$\mathbf{d} = \mathcal{F}(\mathbf{m}) \quad (4)$$

where  $\mathbf{d}$  is the observed data,  $\mathcal{F}$  is the forward operator, and  $\mathbf{m}$  is the model. If the model is known, the forward operator can be used to calculate the expected data (Zhdanov 2002). In geophysical investigations usually the model is unknown and the observed data is used to find the model, which is called an inverse problem (Xue et al. 2020). In practise, the observed data is contaminated with noise, which introduces an error term into the equation ((4)) and thus expands the number of possible models, which can explain the observed data and thus making the inverse problem in geophysics ill-posed and non-linear (Zhdanov 2002). An ill-posed problem means that mathematically there is no or no unique solution (Zhdanov 2002).

Approaches to address this issue can be divided into deterministic and stochastic methods (Xue et al. 2020). The deterministic ap-

proach tries to find a single solution, by iteratively updating the model parameters to minimise the difference between observed and modeled data (Xue et al. 2020). To prevent overfitting to noise, Tikhonov regularisation is used, which adds a penalty term to the least squares problem (Zhdanov 2002), such as:

$$\|\mathbf{W}_d(\mathcal{F}(\mathbf{m}) - \mathbf{d})\|_2^2 + \lambda \|\mathbf{W}_m(\mathbf{m} - \mathbf{m}_0)\|_2^2 \rightarrow \min \quad (5)$$

$\mathbf{W}_d$  and  $\mathbf{W}_m$  are weighting matrices,  $\mathbf{m}_0$  is the initial model, and  $\lambda$  is the regularisation parameter.  $\|\mathbf{W}_m(\mathbf{m} - \mathbf{m}_0)\|_2^2$  can be interpreted as the roughness of the model, which quantifies the complexity or variation of the model (Zhdanov 2002).  $\|\mathbf{W}_d(\mathcal{F}(\mathbf{m}) - \mathbf{d})\|_2^2$  is the data misfit, which quantifies the difference between observed  $\mathbf{d}$  and modeled  $\mathcal{F}(\mathbf{m})$  data and can include an error term (Zhdanov 2002). With the choice of  $\lambda$ , the trade-off between data misfit and model complexity can be controlled (Xue et al. 2020). Building on this foundation, several deterministic methods have been developed, such as Gauss-Newton inversion and Conjugate Gradient (Xue et al. 2020). A constraint inversion can be used to incorporate prior information about the model, which can be used to reduce the number of models able to explain the data, and thus improve accuracy and reliability (Xue et al. 2020).

Stochastic methods, on the other hand, randomly search the solution space and provide a range of plausible models rather than a single deterministic solution (Aigner et al. 2025; Xue et al. 2020). This is significantly more computationally expensive, but can be more robust against noise and can provide uncertainty estimates (Aigner et al. 2025). Particle swarm optimization (PSO) and Bayesian inversion are examples of stochastic methods (Xue et al. 2020).

An implementation of the deterministic approach is the PyGIMLi library, introduced by Rücker et al. (2017), which uses Gauss-Newton inversion to iteratively update the model parameters. PyGIMLi is an open-source library written in Python and C++ and is designed for the inversion of geophysical data (Rücker et al. 2017). PyGIMLi allows the implementation of any given forward operator into the inversion algorithm,

which makes it a versatile tool for geophysical modeling and inversion (Rücker et al. 2017).

#### 2.2.4 L-curve method

Solving inverse problems is a task not limited to geophysics, which makes inversion theory an important field in mathematics (Hansen 1992). There are several methods to solve an inverse problem, but the most common approach is to use Tikhonov regularisation (5) (Zhdanov 2002; Hansen 1992). But the choice of the regularisation parameter  $\lambda$  is not trivial and can have a significant impact on the inversion result (Zhdanov 2002; Hansen 1992).

The L-curve method is widely used to determine the optimal  $\lambda$  for the solution of an inverse problem (Hansen 1992). The L-curve is plotted as a function of its associated residual norm against the solution norm (Hansen 1992). With an increasing  $\lambda$ , the residual norm is expected to increase and the solution norm is expected to decrease, which leads to a curve that resembles an L-shape (Hansen 1992). An optimal  $\lambda$  should minimise the residual norm while keeping the solution norm small. This leads to the “corner” of the L, which is also the point with the highest curvature (Hansen 1992; Farquharson et al. 2004).

Lloyd et al. (1997) implements a method to find the point of maximum curvature and through this the optimal  $\lambda$  for the inversion of diffusion battery data. The method computes the  $\chi^2$ , also called “error weighted root-mean-square”, and the roughness of the model for different  $\lambda$  values to obtain the L-curve (Lloyd et al. 1997). A cubic spline function is fitted to the data points, to make it possible to calculate the curvature for each data point:

$$\mathbf{C}(\lambda_i) = \frac{d^2 s / dx^2}{(1 + (ds/dx)^2)^{3/2}} \quad (6)$$

$$x = \log_{10} \chi^2(\lambda_i)$$

and find the point with the maximum curvature (Lloyd et al. 1997). Lloyd et al. (1997) consider the corresponding  $\lambda$  the optimal one. This method was not developed for geophysical data, but the inversion routine proposed by Aigner et al. (2021) allows for the computation of the model roughness and  $\chi^2$ .

A similar approach was used by Farquharson et al. (2004) to find the optimal  $\lambda$ . In this method the value of the regularization parameter  $\lambda$  is refined in each iteration of the data inversion (Farquharson et al. 2004). Farquharson et al. (2004) start the inversion with a large  $\lambda$  for which an L-curve is calculated. Then the curvature for the chosen  $\lambda$  is calculated through the formula (Farquharson et al. 2004):

$$\begin{aligned} \mathbf{C}(\lambda) &= \frac{\zeta' \eta'' - \zeta'' \eta'}{[(\zeta')^2 + (\eta')^2]^{3/2}} \\ \zeta &= \log \phi_d^{\text{lin}} \\ \eta &= \log \phi_m \end{aligned} \quad (7)$$

$\phi_d^{\text{lin}}$  is the data misfit and  $\phi_m$  is the model roughness. As presented by Farquharson et al. (2004), the next iteration a new  $\lambda$  is calculated based on:

$$\lambda^n = \max(c\lambda^{n-1}, \lambda^{\max}) \quad (8)$$

where  $\lambda^n$  is the new  $\lambda$  value,  $\lambda^{n-1}$  is the previous  $\lambda$  value,  $0.01 \leq c \leq 0.5$  and  $\lambda^{\max}$  is the value for  $\lambda$ , which maximises the curvature. This cooling-schedule-type behaviour is added to prevent the inversion to skip to low values of  $\lambda$ , which is supposed to prevent artifacts created by overfitting the data (Farquharson et al. 2004). This method was tested on synthetic frequency domain electromagnetic data and was able to achieve an appropriate fit to the observed data (Farquharson et al. 2004).

Another approach for finding the optimal  $\lambda$  is the iterative golden section search as proposed by Cultrera et al. (2020). The authors propose to define an initial range for the optimal  $\lambda$   $[\lambda_1, \lambda_4]$ , two more  $\lambda$  values are calculated using the formula:

$$\begin{aligned} \varphi &= \frac{1 + \sqrt{5}}{2} \\ \lambda_2 &= 10^{\frac{\log_{10} \lambda_4 + \varphi \cdot \log_{10} \lambda_1}{1 + \varphi}} \\ \lambda_3 &= 10^{\log_{10} \lambda_1 + (\log_{10} \lambda_4 - \log_{10} \lambda_2)} \end{aligned} \quad (9)$$

For each  $\lambda$  the corresponding point on the L-curve is found and two curvatures ( $C_2$  and  $C_3$ ) are computed relying on three points each.  $C_2$  is the curvature of the points  $\lambda_1, \lambda_2$ , and  $\lambda_3$ .  $C_3$  is the curvature of the points  $\lambda_2, \lambda_3$ , and  $\lambda_4$  (Cultrera et al. 2020). Then Cultrera

et al. (2020) omitted  $\lambda_1$  or  $\lambda_4$  depending on which curvature is larger and a fourth  $\lambda$  is calculated based on the formula for  $\lambda_2$  (9). This process is repeated until the difference between the lambda-values of the interval are below a certain threshold (Culturera et al. 2020). Cultrera et al. (2020) state that this method allows to find an optimal  $\lambda$  while minimising the number of inversions necessary. The search algorithm was tested with the ERT method on a conductive thin film with two non-conductive anomalies and showed promising results in finding the "corner" of the L-curve (Culturera et al. 2020).

### 2.3 Experimental Set Up

In order to investigate the applicability of automatically determining an optimal lambda value to TEM data, we conducted a field survey in October of 2024 at the Martenhofer Lacke in the Nationalpark Neusiedlersee - Seewinkel. Existing data available at the Geophysics Research Unit at TU Wien from May 2024 for the same location, but with a differing measuring configuration was also made available for this thesis, which enables a comparison between varying setups.

In frame of this thesis a python package was developed to read, filter, and invert the TEM data. The visualisation of an L-curve as well as three techniques of automatically finding an optimal lambda were also implemented. Namely the cubic spline method based on Lloyd et al. (1997), an similar approach using the `gradient()` function from the `numpy` library, and the golden section search as proposed by Cultrera et al. (2020).

#### 2.3.1 Measuring Device

Field surveys were conducted with the TEM-Fast 48 HPC system by Applied Electromagnetic Research (AEMR), which is compact device allowing the use of a single-loop configuration (Barsukov et al. 2006; Aigner et al. 2021). By connecting an external 12 / 24 V battery a current either 1 / 4 A can be put through the connected transmitter loop (Aigner et al. 2021). It records up to 48 logarithmically spaced time gates, which results in a time range between 4 – 16000  $\mu$ s (Aigner et al. 2021). The

specific number of time gates can be chosen through a time-key (Aigner et al. 2021). Table 2 shows which time-key leads to which recording time range ((Excerpt from the manual of the TEM-FAST 48 system)). To provide an optimal signal-to-noise ratio the device automatically stacks multiple pulses (Barsukov et al. 2006). The number of stacks are given by the formula  $P_{tot} = 13 \times n_s \times n_{as}$  (Aigner et al. 2021), where  $n_s$  (1 – 20) is the chosen stacking-key and  $n_{as}$  is the number of analogue stacks depending on the chosen time-key and can be found in Table 2. More detailed information on the device can be found in the manual provided on the website <http://www.aemr.net/tem-fast.htm>.

#### 2.3.2 Field Survey

The field measurements were carried out at the Martenhofer Lacke in the *Nationalpark Neusiedlersee - Seewinkel* ( $16^{\circ} 51' 23.058''$  N,  $47^{\circ} 45' 8.4348''$  E), which is located on the east side of the Neusiedler See, Austria. Being part of the Seewinkel, which are intermittent alkaline soda waters, this water cycle of this lake is fueled by deep saline groundwater and evaporation leading to its high salinity and shallow water depth, which also varies throughout the year (Boros et al. 2025). This location was chosen due to the lack of man-made structures in the Nationalpark, which reduces noise in the gathered TEM data to a minimum (Aigner et al. 2024).

The first survey, consisting of 45 soundings as shown in Figure 2 with a  $12.5 \times 12.5$  m loop, was carried out on the 22nd May 2024 and for the second survey 66 soundings, visualised in Figure 3 with a  $6.25 \times 6.25$  m loop were measured on 8th October 2024. For both surveys a voltage of 24 V was used and Table 3 shows the parameters for each sounding. Based upon a first visual inspection of the data some soundings were marked as "anomalous" as seen in Figures 2 and 3.

#### 2.3.3 Python Package

In order to process the gathered data, we developed a python package mainly based on open-source python libraries. For the inversion routine we built upon the work of Aigner et al. (2021), which combines the electromagnetic

**Tab. 2:** Parameters relating to the time-key of the TEM-FAST 48 HPC system (Excerpt from the manual).

Key	Max Time ( $\mu\text{s}$ )	Time Gates	Analogue Stacks
1	64	16	1024
2	128	20	512
3	256	24	256
4	512	28	128
5	1024	32	64
6	2048	36	32
7	4096	40	16
8	8192	44	8
9	16384	48	4

**Tab. 3:** Device settings used as well as the resulting measured time ranges and total number of pulses stacked for each sounding of both surveys.

Sounding	Current	Time Range	Time Key	Stacking Key	Total Stacks
<b>22nd May 2024</b>					
M001, M002	4.1 A	4 – 480 $\mu\text{s}$	4	3	4992
M003 – M014	1.0 A	4 – 480 $\mu\text{s}$	4	3	4992
M015 – M045	1.0 A	4 – 240 $\mu\text{s}$	3	3	9984
<b>8th October 2024</b>					
M001 – M066	4.1 A	4 – 240 $\mu\text{s}$	3	5	16640

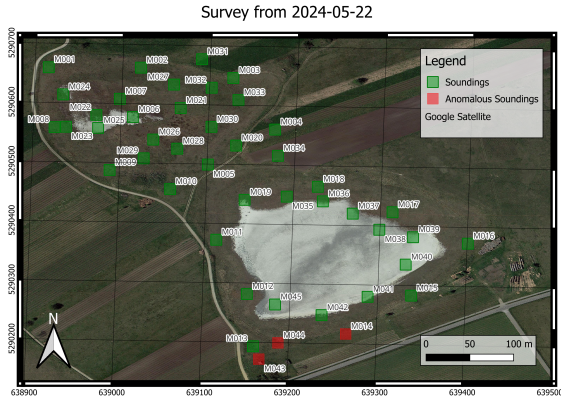


**Fig. 2:** Locations of all the TEM soundings measured in the first survey (22nd May 2024), where soundings are marked as anomalies, which fell out of order in a first visual inspection.

wave modelling capabilities of `empymod` (Werthmüller 2017) with the inversion algorithm from `PyGIMLi` (Rücker et al. 2017).

The capabilities of this package include the reading of TEM data, adding coordinates to

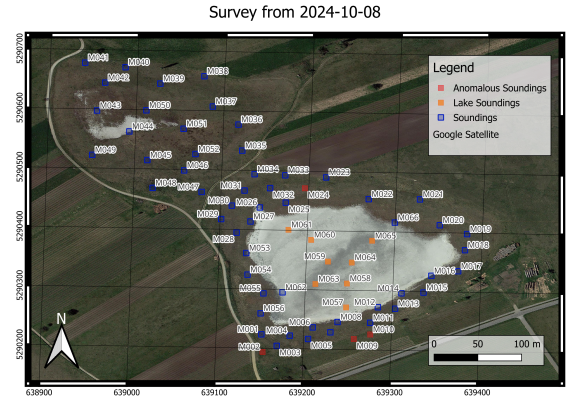


**Fig. 3:** Locations of all the TEM soundings measured in the second survey (8th October 2024), where soundings are marked as anomalies, which fell out of order in a first visual inspection.

each sounding, the filtering based upon a time interval, and the visualisation of the raw with the filtered data. The inversion routine requires certain starting parameters like the regularisation parameter  $\lambda$ , a layer distribution, a start

model, and the relative error of the measured signal. If not specified otherwise a homogeneous model with the median apparent resistivity of the sounding is used as the starting model and the relative error is computed based of the error output of the measuring device. In case of particularly noisy data it is possible to set a minimum value for the relative error (noise floor). The noise floor can also set to entirely replace the recorded errors with a constant error vector, like Aigner et al. (2021) proposed. The relative error limits how strongly the inversion algorithm tries to fit the model to each data point to avoid fitting errors. This inversion algorithm works with a model of the subsurface, where a resistivity value is assigned to a layer with a certain thickness, and only modifies the resistivity value of every layer while keeping the thicknesses fixed. This makes the choice of an appropriate layer distribution (specifying the number and thicknesses of layers) vital (Welkens 2025).

The python routine described in this thesis computes and visualises an L-Curve for a TEM sounding. For this we run the inversion for various logarithmically spaced lambda values, specified by the lower bound, the upper bound, and the number of values. For each inversion, we compute the root-mean-square (RMS) misfit of the data with the model as well as the roughness of the model and use these two values as the coordinates of a point corresponding to each inversion, which should result in an L-Curve (Cultrera et al. 2020; Hansen 1992).

To find an optimal lambda value for the inversion we implemented three search algorithms, which all try to find the point (corresponding to a lambda value) with the highest curvature on the L-Curve (Lloyd et al. 1997; Cultrera et al. 2020). We implemented the method used by Lloyd et al. (1997), which fits a cubic spline function to the L-Curve and computes the first and second derivative of this function, which are used to compute the curvature of the function at each point. We also implemented a similar approach, where we used the `numpy.gradient()` function (<https://numpy.org/doc/1.26/reference/generated/numpy.gradient.html>) to compute the first and second derivative for the curvature. Lastly we implemented the iterative

golden section search algorithm as described by Cultrera et al. (2020), where a lower and upper bound is defined for the lambda value and by comparing two curvatures within the interval and discarding the lower one, this method contracts the interval towards the optimal lambda. The advantage compared to the other two methods is that it is not bound to the predefined list of logarithmically spaced lambda values, which in theory allows a more precise determination of the optimal lambda.

## 3 Results

The raw data were plotted in terms of the measured secondary magnetic field ( $\frac{V}{m^2}$ ), referred to as “impulse response” in this thesis, and the conversion to apparent resistivity  $\rho_a$  ( $\Omega m$ ), using Equation (1). The latter reveal larger contrasts and permit an easier visual identification of outliers. The data gathered in the two surveys was processed separately.

### 3.1 Filtering of the Data

After plotting, the soundings of the first survey (22nd May 2024) were split into two groups: “Clean” and “noisy” data, with noisy referring to sounding close to the road (“M014”, “M043”, and “M044” as seen in Figure 2). The noisy soundings are likely related to measurements affected by interferences of possible anthropogenic structures and parasitic electromagnetic fields contaminating the data (Christiansen et al. 2006). Figure 4 shows the clean soundings of the first survey (22nd May 2024) with the  $12.5 \times 12.5$  m loop and Figure 5 shows the noisy data. In Figure 4(b) it can be clearly seen that the effects of the turn-off ramp as described by Aigner et al. (2021) influence the measurements until about  $8 \mu s$ , which is consistent with the  $4.2 - 8.6 \mu s$ , found by Aigner et al. (2021) for conductive media. At about  $240 \mu s$  Figure 4(b) shows how the various curves start having distortions and Figure 4(a) shows that measured impulse responses are becoming a similar order of magnitude as the measured errors. For this reason the measurements were filtered by excluding all time gates outside of the time range of  $8 - 210 \mu s$  as shown in Figure 4(c) and (d). Figure 4(d) shows the pattern, that the  $\rho_a$  values first de-

crease for most soundings and start increasing for all soundings for a time larger than  $30\ \mu\text{s}$ .

The apparent resistivities of the noisy soundings as seen in Figure 5(b) show no clear pattern due to high distortions in the curves. The anomalous measurements shown in Figure 5 were still processed, to test how well they compare to the other soundings. In order to make it more comparable the same time range of  $8 - 210\ \mu\text{s}$  was used for the filtering (Figure 5(d)).

The clean soundings (Figure 6) and anomalies (Figure 7) of the second survey (8th October 2024) with the  $6.25 \times 6.25\ \text{m}$  loop were processed in a similar way. Comparing Figure 6(b) with Figure 4(b) shows that the effects of the turn-off ramp both end at  $8\ \mu\text{s}$ , while the distortions in the data from the second survey start earlier at  $100 - 110\ \mu\text{s}$ . The impulse response also becomes the same order of magnitude as the measured error (Figure 6(a)) at the same time ( $110\ \mu\text{s}$ ). Thus all the time gates outside the time range  $8 - 110\ \mu\text{s}$  were filtered as shown in Figure 6(c) and (d). Figure 6(d) shows that in contrast to the soundings with the larger loop (Figure 4(d)), the  $\rho_a$  values do not decrease in the early times, but also start increasing after  $30\ \mu\text{s}$ .

The noisy soundings shown in Figure 7 can be divided into two groups: Measurements close to man-made structures, such as the road (“M002”, “M009”, “M010”, and “M024” as seen in Figure 2), which show similarities to the noisy soundings of the first survey (Figure 5(b)). “M002”, “M009”, and “M010” show significantly lower apparent resistivity values, than the other soundings – at  $40\ \mu\text{s}$   $10\ \Omega\text{m}$  (Figure 7) instead of  $20\ \Omega\text{m}$  (Figure 6). This could be due to coupling effects, as the impulse response curves (Figure 7(a)) look similar to the example for capacitive coupling described by Christiansen et al. (2006). “M024” shows higher a apparent resistivity of  $30\ \Omega\text{m}$  at  $40\ \mu\text{s}$  and a much steeper increase in the  $\rho_a$  values (Figure 7)

Measurements within the lake (“M057”-“M065”, except for “M062”, as seen in Figure 2), which show effects of the turn-off ramp until  $12\ \mu\text{s}$  (Figure 7(b)). For these sounding the loop was submerged in the lake (up to  $30\ \text{cm}$  deep), where the water is a good conductor due to its high salinity with resistivities of  $0.78 - 7.16\ \Omega\text{m}$  (Boros et al. 2025). This also

breaks the assumption of a layered half-space, which is necessary for the inversion of TEM data (Christiansen et al. 2006), and thus all soundings within the lake (marked orange in Figure 3) were excluded from further processing.

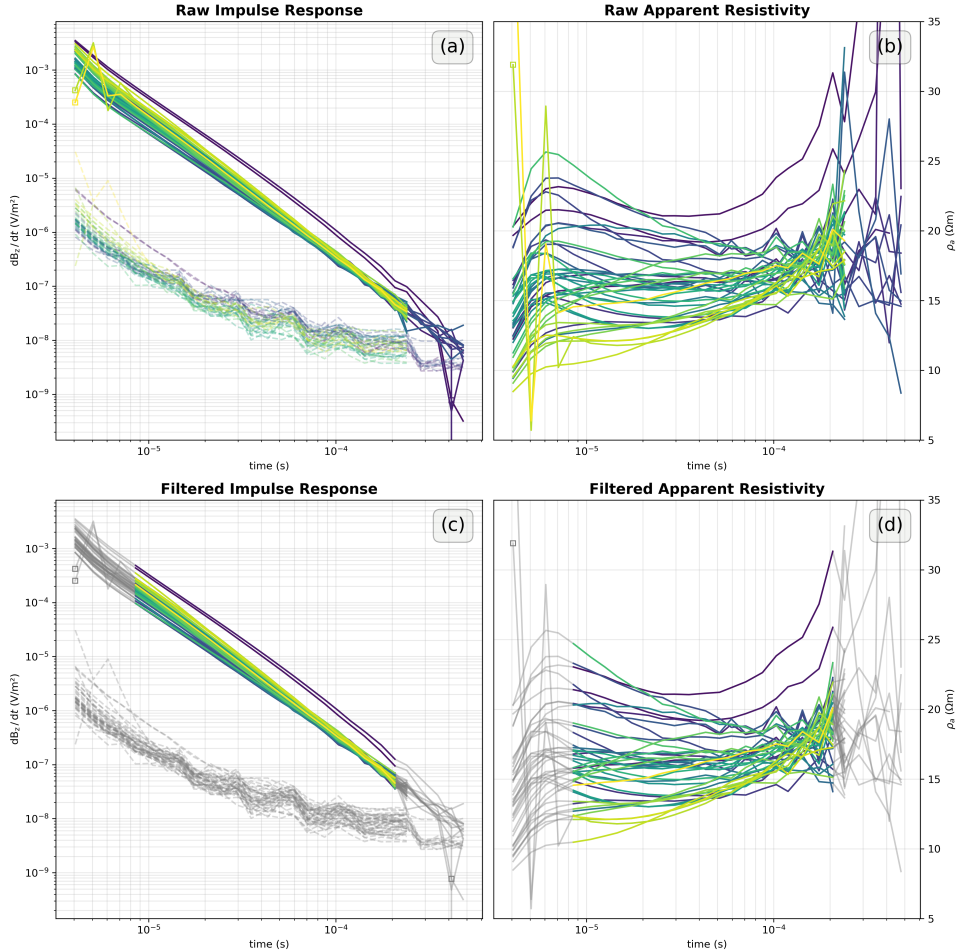


**Fig. 4:** Raw and filtered impulse responses and apparent resistivities from the 22nd May 2024 survey, where anomalies are excluded. The first sounding (M001) is colored dark purple, the last sounding (M045) is yellow, and all soundings in between are assigned a color from a uniform distribution between the two border colors. Subfigure (a) shows the raw impuls response as well as the measured errors as dashed lines, (b) shows the computed apparent resistivities, (c) show the filtered impulse response, the measured error as dashed lines, and greyed out raw data as comparison, (d) shows the resulting filtered apparent resistivities and greyed out raw values.

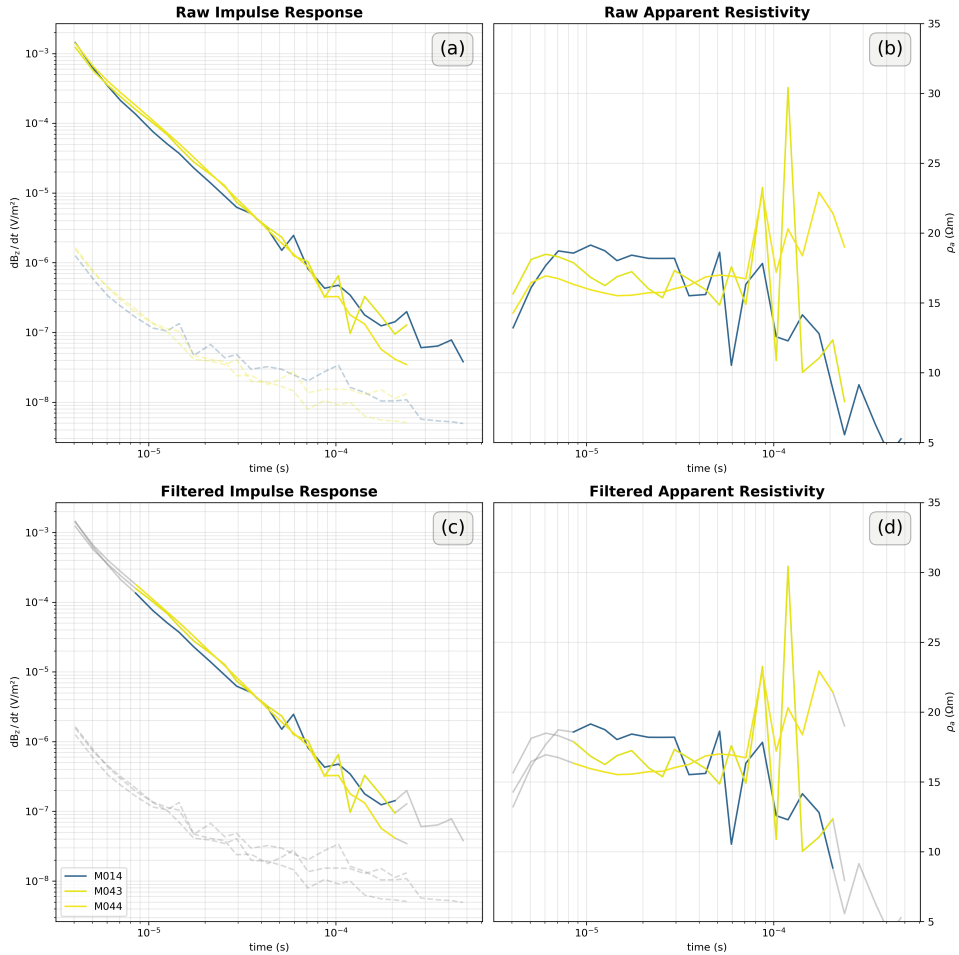


**Fig. 5:** The anomalous raw and filtered impulse responses and apparent resistivities from the 22nd May 2024 survey. Subfigure (a) shows the raw impuls response as well as the measured errors as dashed lines, (b) shows the computed apparent resistivities, (c) show the filtered impulse response, the measured error as dashed lines, and greyed out raw data as comparison, (d) shows the resulting filtered apparent resistivities and greyed out raw values.

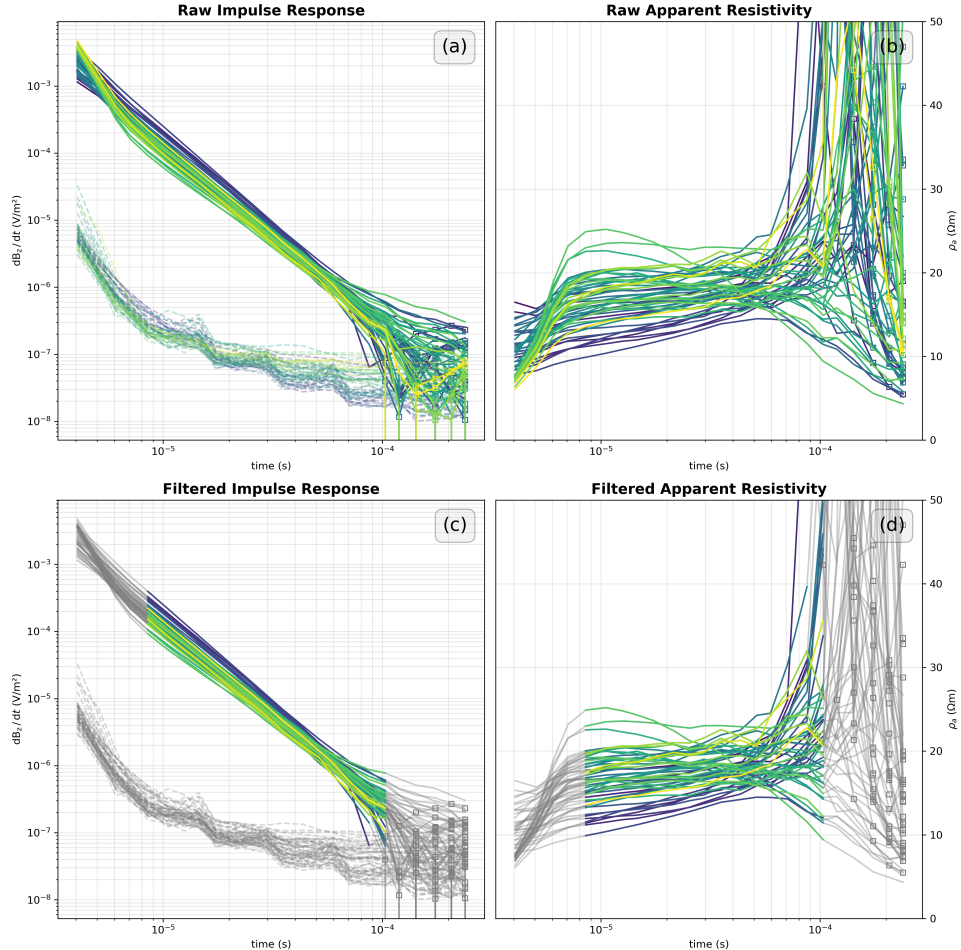


**Fig. 6:** Raw and filtered impulse responses and apparent resistivities from the 8th October 2024 survey, where anomalies are excluded. The first sounding (M001) is colored dark purple, the last sounding (M066) is yellow, and all soundings in between are assigned a color from a uniform distribution between the two border colors. Subfigure (a) shows the raw impuls response as well as the measured errors as dashed lines, (b) shows the computed apparent resistivities, (c) show the filtered impulse response, the measured error as dashed lines, and greyed out raw data as comparison, (d) shows the resulting filtered apparent resistivities and greyed out raw values.

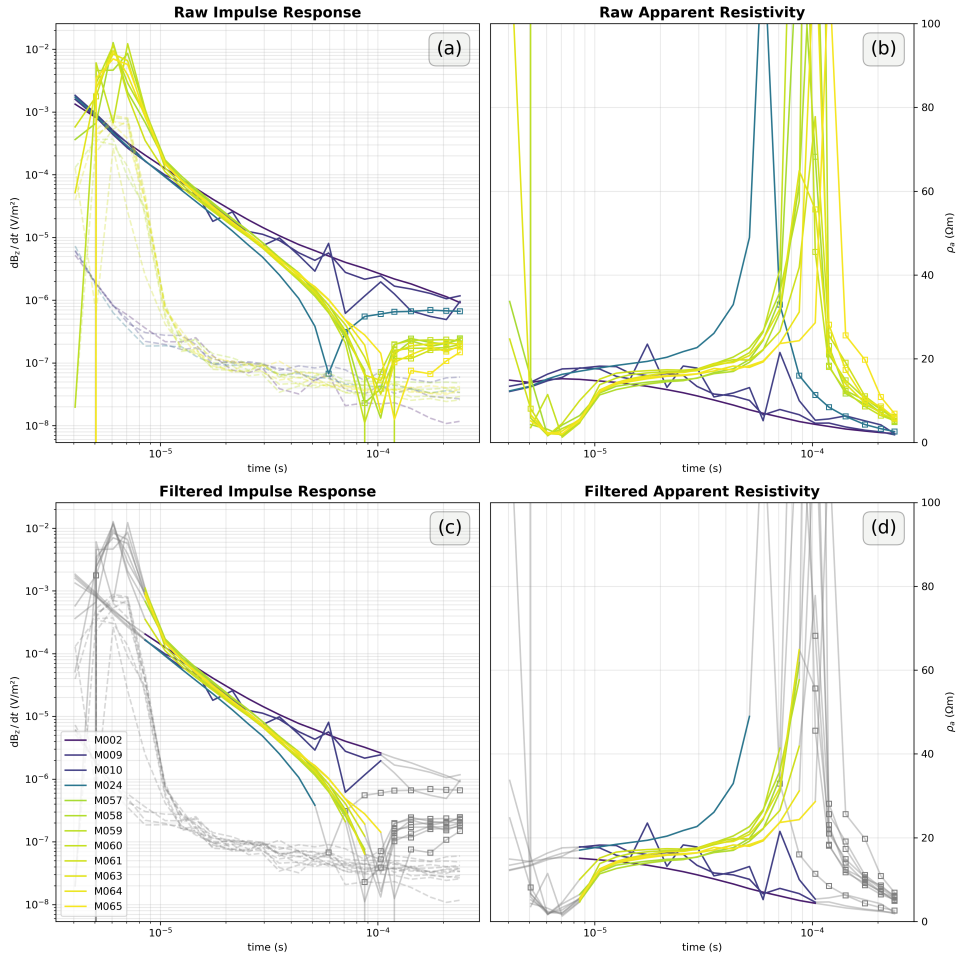


**Fig. 7:** The anomalous raw and filtered impulse responses and apparent resistivities from the 8th October 2024 survey. Subfigure (a) shows the raw impuls response as well as the measured errors as dashed lines, (b) shows the computed apparent resistivities, (c) show the filtered impulse response, the measured error as dashed lines, and greyed out raw data as comparison, (d) shows the resulting filtered apparent resistivities and greyed out raw values.

### 3.2 Inversion Parameters

In this section we evaluate the effect in the inversion due to varying parameters, which are necessary for the algorithm by Aigner et al. (2021): The relative error vector, range of  $\lambda$  values, and the layer distribution. The relative error vector specifies the corresponding relative error for each recorded impulse response of a time gate. It can be derived from the absolute errors, which the device records automatically or set manually. Aigner et al. (2024) conducted a survey at the same location with a  $50.0 \times 50.0$  m loop and found that the device overestimates the error.

Thus Aigner et al. (2024) used a constant 1.5 % relative error vector for the inversion. For the data collected in both surveys of this thesis, the inversions were run defining an relative error vector of 1.5 %.

The inversion algorithm of Aigner et al. (2021) also requires a regularisation parameter  $\lambda$ . This thesis focusses on finding an optimal  $\lambda$  by using the L-Curve method. The L-Curve method was implemented in a way, that it requires an interval of two  $\lambda$  values, which are used to create a range 20 of logarithmically spaced  $\lambda$  values. These are then used to compute 20 inversions of which the corresponding RMS misfit and model roughness is plotted to create the L-Curve. The study from Aigner et al. (2024) uses  $\lambda$  values between 40.5 – 50 for the inversion. To allow divergence from these values, a lower bound of 5 and an upper bound of 100 was chosen for this thesis.

The layer distribution specifies the number and thicknesses of the layers characterising the subsurface model, which is used for the inversion. Welkens (2025) shows that a layer model with 1 m-Layers until 5 m depth and 1.5 m-Layers below that, until a maximal depth of 10 m optimises the inversion speed and model fit for data gathered with a  $6.25 \times 6.25$  m loop and 4.1 A of current. For a first survey of this thesis a  $12.5 \times 12.5$  m loop was and using Figure 8(c) shows that the inversion algorithm struggles to fit the late time data, when using the layer distribution suggested by Welkens (2025). Figure 9(c) shows that this issue can be resolved by choosing a maximal depth of 20 m and keeping the other layer thickness suggestions from Welkens (2025). The visual differences between Figure 8(c) and Figure 9(c) are minimal, and thus the relative root-mean-square (RMS) of the misfit between modelled and observed data was used to quantify the improvement, which decreased from 2.32 % to 2.09 % using 20 m instead of 10 m as the maximal depth.

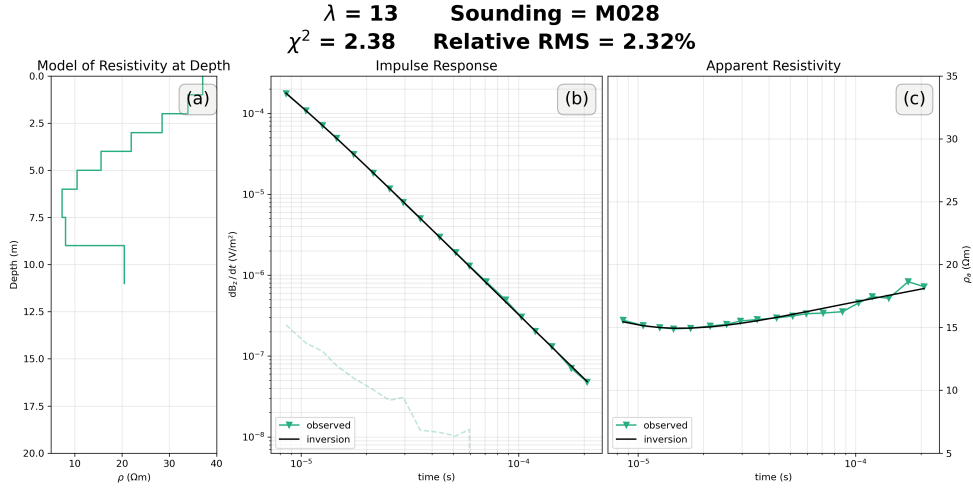


**Fig. 8:** Inversion results for a representative sounding (M028) for the first survey (22nd May 2024) with the layer distribution of 1 m thicknesses until 5 m depth and 1.5 m until 10 m depth. Subfigure (a) shows the final subsurface model of the resistivity, (b) shows the comparison between the modelled and measured impulse response as well as the measured error as a dashed line, (c) shows the comparison between the modelled and measured apparent resistivities.

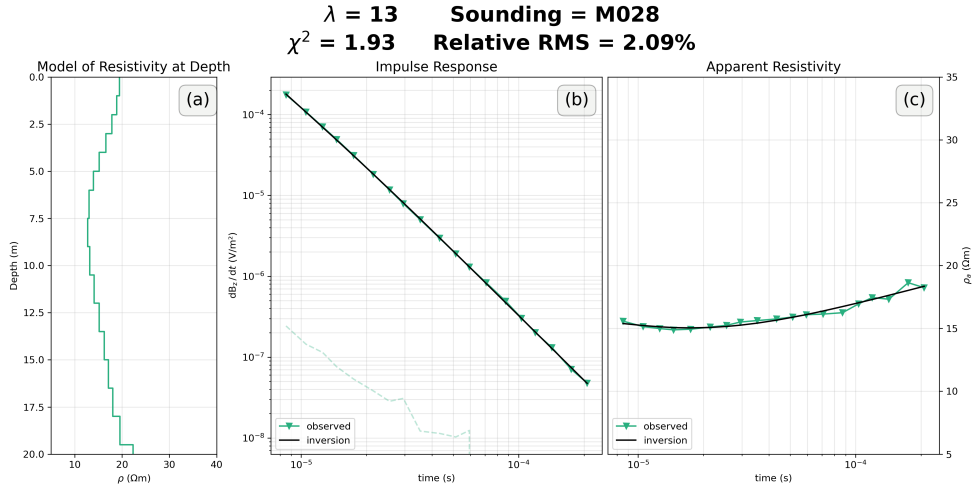


**Fig. 9:** Inversion results for a representative sounding (M028) for the first survey (22nd May 2024) with the layer distribution of 1 m thicknesses until 5 m depth and 1.5 m until 20 m depth. Subfigure (a) shows the final subsurface model of the resistivity, (b) shows the comparison between the modelled and measured impulse response as well as the measured error as a dashed line, (c) shows the comparison between the modelled and measured apparent resistivities.

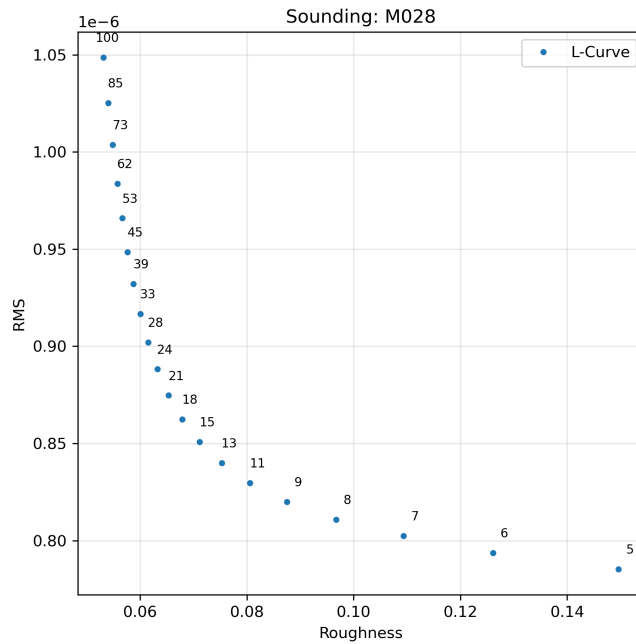
### 3.3 The L-Curve Method

The L-Curve technique can be used to plot the model roughness against the model misfit for varying regularisation parameter ( $\lambda$ ) values, which can be used to find the optimal lambda  $\lambda_{\text{opt}}$  (Hansen 1992). This can be done by visually finding the “corner” of the L-curve, which were computed with the parameters from Section 3.2: 1.5 % as the relative error, 20 logarithmically spaced  $\lambda$  values in the range 5 – 100, and the layer distribution from Welkens (2025) but with a maximal depth of 20 m. For the first survey the L-Curves were computed for the clean as well as noisy soundings, where we found no significant visual difference between the clean and noisy data, and thus excluded all noisy data from further analysis. The remaining 43 soundings of the first survey were manually analysed and we were able to find an optimal lambda  $\lambda_{\text{opt}}$  for 83.33 % of the soundings. Doing the same for the 54 clean soundings of the second survey resulted in finding a  $\lambda_{\text{opt}}$  for 66.67 % of the soundings.

Figures 10 and 11 show two L-Curves, which allowed finding an  $\lambda_{\text{opt}}$ . Figure 10 shows the L-Curve for the sounding “M028” of the first survey and illustrates the expected L-Curve as it is described by Hansen (1992). Based on Figure 10 we determined the optimal lambda

for this sounding to be at 13, which minimises both the RMS misfit and the model roughness. Figure 11 shows the L-Curve for the sounding “M003” of the second survey and was selected to showcase how the computed L-Curve can deviate from the expected ideal, but still provide useful information. Figure 11 shows contrary to what is expected, the RMS misfit increases between lambdas 8 – 5 and decreases between 63 – 100, but the curve still has the characteristic “corner” at the  $\lambda$  value 8, which we determined to be the optimal lambda.

Figures 12 and 13 show two examples of the L-Curve method not working to find an optimal lambda for TEM soundings. Generally for an increasing  $\lambda$  a decreasing model roughness and an increasing model misfit is expected (Hansen 1992), but Figure 12, which was calculated for the sounding “M045” of the first survey, shows a decreasing model misfit (RMS misfit) for an increasing  $\lambda$ . It is plausible that this behaviour changes with further increases in the  $\lambda$  values, as it happens in Figure 11 between 8 – 53. Figure 13 shows an example, which was computed for the sounding “M019” of the second survey, where the L-Curve method produced no cohesive curve, but rather collection of seemingly randomly positioned points.



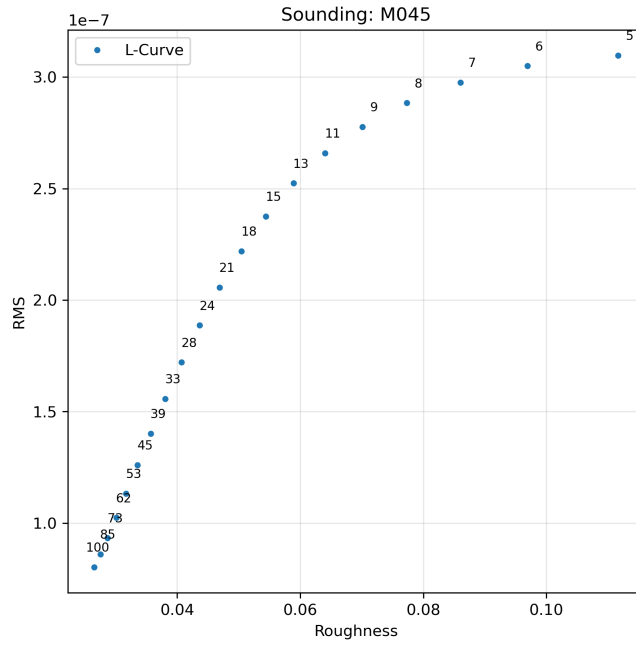


**Fig. 12:** L-Curve of the sounding M045 in the first survey (22nd May 2024), which shows an increasing RMS with an increasing roughness, which is the opposite to the expected characteristics of a L-Curve.

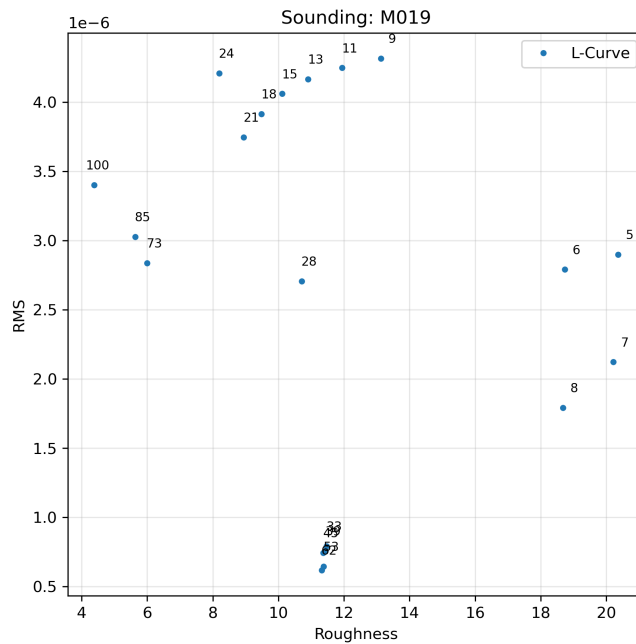


**Fig. 13:** “L-Curve” of the sounding M019 in the second survey (8th October 2024), which shows a seemingly random collection of points instead of a L-Curve.

### 3.4 Finding an Optimal Lambda

The clean soundings of both surveys were used to test the three search algorithms presented in Section 2.3.3: All algorithms try finding the  $\lambda$  corresponding to the point on the L-Curve with the maximal curvature. The “cubic-spline” based approach fits a cubic spline function, which is then used to compute the curvatures of each point (Lloyd et al. 1997). The “gradient-based” method utilises the `gradient()` function from the `numpy` library to achieve the same. The “golden section search” is an iterative search algorithm based on Cultrera et al. (2020).

In early versions all three search algorithms performed poorly and we attributed this to the fact that the RMS misfit and the model roughness are 5 – 6 orders of magnitude apart, which can be seen when looking at the axis of Figure 11. Figure 14 shows how all three search algorithms return a  $\lambda$  between 41 – 62, which is higher than the visually determined  $\lambda_{\text{opt}}$  at 13. To counteract this a linear normalisation, using the formula  $a_i = \frac{a_i - a_{\min}}{a_{\max} - a_{\min}}$ , was applied to both RMS and roughness. Figure 15 shows how with the normalisation all three search algorithms return a value (12 – 15) around the visual optimum of 13. Hence all further searches

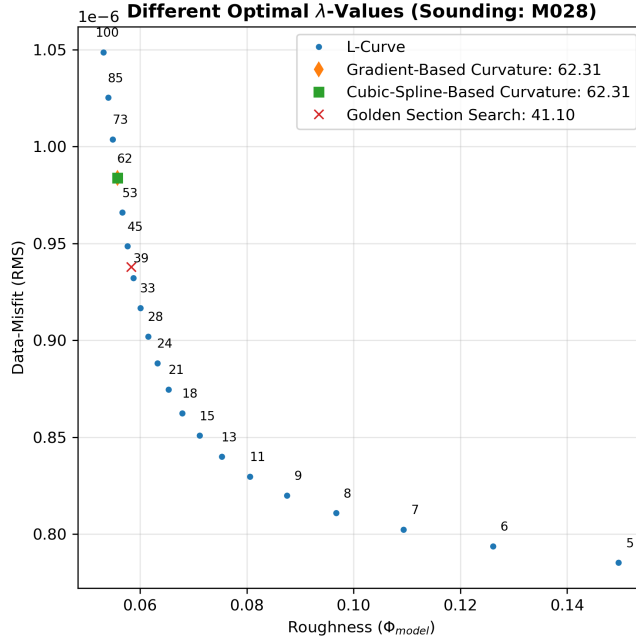
for an optimal lambda were carried out with the normalisation.

Figure 15 demonstrates that all three search algorithms are able to find the optimal lambda for a L-Curve, which resembles an ideal L-Curve as described by Hansen (1992). Figure 17 shows that all three search algorithms find the optimal lambda at 8 when there is a clear point with a maximal curvature, even if the L-Curve deviates from the expected ideal. Figure 16 demonstrated how the various search algorithm find different “optimal” lambda values, when the curvature of the computed L-Curve has no distinct maximum, which is exemplified by sounding “M020” of the first survey. When inspecting the L-Curve shown in Figure 16, we determined  $\lambda_{\text{opt}}$  to be 15: The “cubic-spline” and “gradient” based search algorithms overestimated  $\lambda_{\text{opt}}$  to be between 45 – 53, while the “golden section search” underestimated  $\lambda_{\text{opt}}$  to be 7.

These examples highlight the strengths and shortcomings of each search algorithm. Table 4 shows a summary of how the algorithms performed overall and comparing this to a visual inspection of the generated L-Curve. The L-Curve method worked for 83.33 % of the soundings with the first survey and only for 66,67 % of the soundings with the second survey. Table 4 shows that this trend continues for the performance of the search algorithms. We evaluated each search algorithm by comparing the obtained  $\lambda$  with our visual analysis from Section 3.3.

We classified an automatic search “successful”, if the returned  $\lambda$  was within an interval of 15 % around the  $\lambda_{\text{opt}}$  from our manual inspection. Table 4 shows that for the first survey the “Golden Section Search” was more successful at finding the  $\lambda$  with 74.29 % than the “Gradient Based” approach with 71.43 %, while for the second survey the Gradient Based method worked better with 47.22 % than the Golden Section Search with 41.67 %. Throughout both surveys the “Cubic Spline” based search performed the worst with 60.00 % for the first and 33.33 % for the second survey.

We also computed the means of the relative deviations between the visually obtained  $\lambda$  and the automatically computed value for each search algorithm. We introduced this metric



**Fig. 14:** Automatically searching for an optimal lambda of the sounding M028 in the first survey (22nd May 2024) without applying a normalisation to the L-Curve.

beside the binary “Successrate” to quantify the reliability of each search algorithm: By measuring the mean deviations, we not only see if the  $\lambda_{\text{opt}}$  was found, but also how far off the lambda searches were on average. Table 4 shows that the Gradien Based approach had the lowest mean relative deviations with 15.89 % (first survey) and 39.57 % (second survey). The Golden Section Search deviated the second least for the first survey with 17.55 %, but performed the worst for the second survey with 118.28 %. The Cubic Spline method showed a mean relative deviation of 32.66 % for the first survey and 65.21 % for the second.

**Tab. 4:** Summary of the search for an optimal lambda for each sounding, comparing the visual identification with the various automated search algorithms.

Search Type	Successrate (%)	Mean relative deviation (%)
<b>22nd May 2024</b>		
Visual	83.33	-
Cubic Spline	60.00	32.66
Gradient Based	71.43	15.89
Golden Section	74.29	17.55
<b>8th October 2024</b>		
Visual	66.67	-
Cubic Spline	33.33	65.21
Gradient Based	47.22	39.57
Golden Section	41.67	118.28

All comparison plots can be found at [https://github.com/pb-tuwien/BSc\\_Soda\\_Lakes\\_Balogh.git](https://github.com/pb-tuwien/BSc_Soda_Lakes_Balogh.git) under "data/2024xxxx/TEMdata/07-inversion\_analysis/comparison\_M0yy.png", where xxxx is either "0522" for the first or "1008" for the second survey and yy being the sounding number (either 01 to 45 or 01 to 66 – exluding the numbers for the noisy soundings). A consistant trend throughout our analysis of the search algorithms (Table 4) is that the second survey performed better for the L-Curve method, than the first survey.

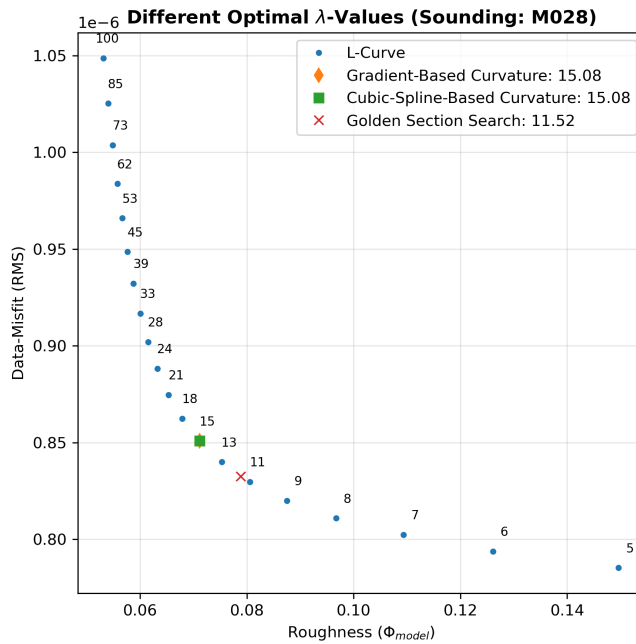


**Fig. 15:** Automatically searching for an optimal lambda of the sounding M028 in the first survey (22nd May 2024) while applying a normalisation to the L-Curve.

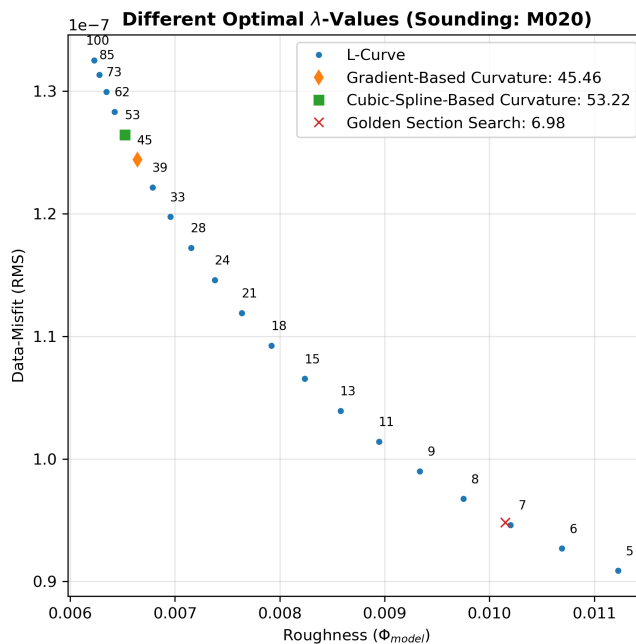


**Fig. 16:** Automatically searching for an optimal lambda of the sounding M020 in the first survey (22nd May 2024), which showcases how performance the different search algorithms deviate.

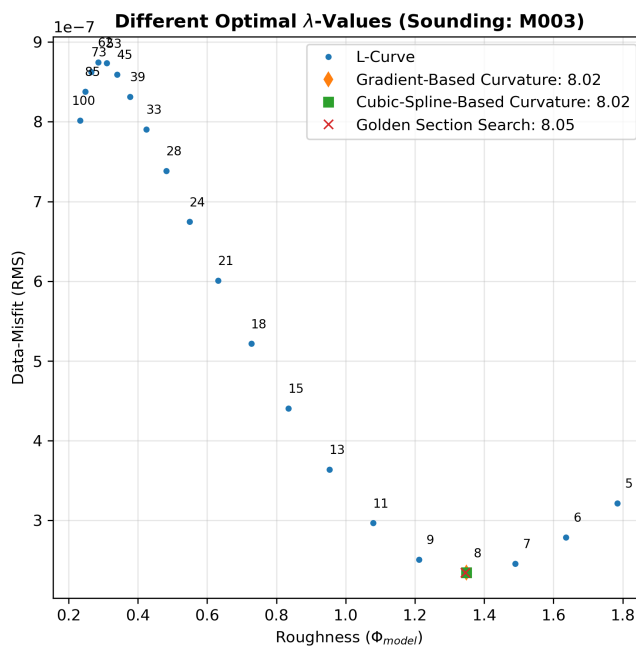


**Fig. 17:** Automatically searching for an optimal lambda of the sounding M003 in the second survey (8th October 2024), which showcases how the different search algorithms perform well, even when the computed L-Curve deviates from the theoretical ideal, but some expected characteristic of an L-curve can be found.

### 3.5 Comparing Inversion Results

#### REVISED UNTIL HERE

With these findings, we finally obtained the necessary parameters for running the inversions, which enables a comparison of different resistivity models obtained from the various measuring configurations, as described in Table 3. Because the late time data was filtered due to a high noise level, the different time keys are not considered and only the different injected currents and the loop sizes are compared. Ideally the compared soundings, would be at the same location, which is why we chose the soundings M028 (shown in Figure 18) of the first and M052 (shown in Figure 19) of the second survey, which use the  $12.5 \times 12.5$  m loop with 1.0 A of current and  $6.25 \times 6.25$  m loop with 4.1 A of current. Figures 2 and 3 show that these two broadly align. For the configuration  $12.5 \times 12.5$  m loop with 4.1 A of current we do not have a sounding at the same location, but sounding M002 (shown in Figure 20) of the first survey is also in the north of the Martenhofer Lacke (Figure 2). Figure 18(c) shows how with the large loop three distinct layers can be found: A 5 m-layer with  $17.5 \Omega\text{m}$ , a second 11 m-layer with  $13.5 \Omega\text{m}$ , and the start of a third layer with  $22 \Omega\text{m}$ . The model seems to fit the data adequately as can

be seen in Figure 18(a) and (b), which is also supported by a relative RMS misfit of 4.77 %.

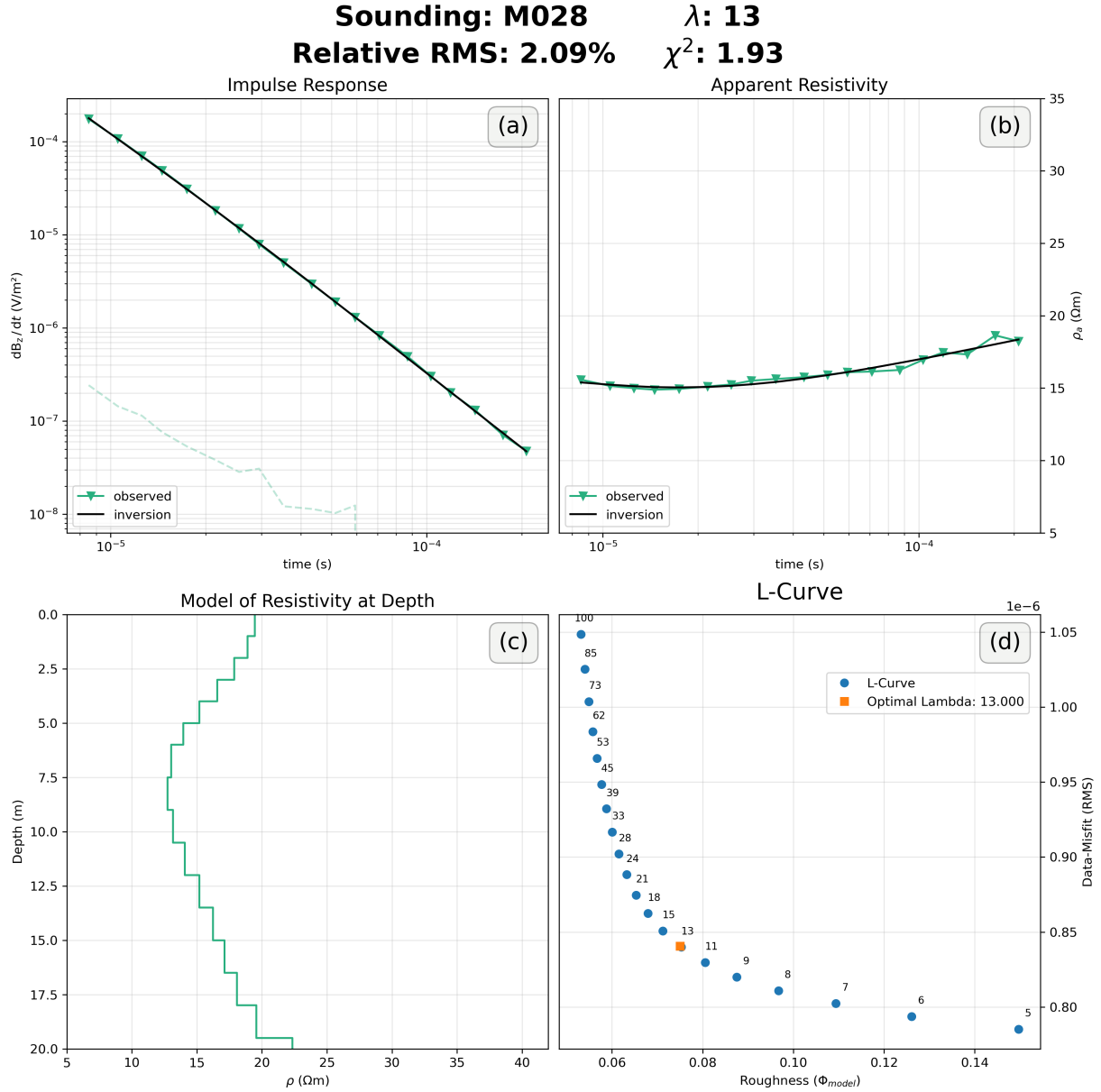
For the same location five months later the small loop with 4.1 A produces a model with only two discernable layers, as seen in Figure 19(c): A 5 m-layer with  $16 \Omega\text{m}$  and the start of a second layer with  $24 \Omega\text{m}$ . The second layer is not distinctly visible, but rather a gradual increase, which corresponds with the almost linearly increasing apparent resistivity curve in Figure 19(b). Figure 19(a) and (b) also show that the last measured data point possibly indicates a change in the slope and thus a new layer (Fitterman et al. 1986), but it could also be data noise.

Figure 20 represents the measurements made with the large loop as well as 4.1 A and in (c) similar three layers can be seen as in Figure 18(c) but with differing resistivity values: A 5 m-layer with  $31 \Omega\text{m}$ , a second 12 m-layer with  $13.5 \Omega\text{m}$ , and the start of a third layer with  $30 \Omega\text{m}$ . Figure 20(b) shows that the model does not quite fit the measured data, but follows the general trend of the curve.

We found that the measurements with the  $12.5 \times 12.5$  m loop were able to discern the same three layers regarding the thicknesses, which Aigner et al. (2024) found in a borehole at the soda lakes, which is located about 1.5 km northeast of the Martenhofer Lacke. Aigner et al. (2024) describes a 1.6 m clay-silt layer, followed by a 5.4 m sandy gravel aquifer, and a second clay-silt layer until the maximal drilled depth of 10 m. Figures 18 and 20 both show in subfigure (c) that the first two layers of the borehole can not be differentiated and are shown as one layer with the resistivities of  $31 \Omega\text{m}$  and  $17.5 \Omega\text{m}$  respectively. These differences could be caused by differing clay-silt layer and aquifer thicknesses, which also changes the influence of each over the resistivity value representing the combined resistivities of both layers. The second layer present in the subfigures (c) of Figures 18 and 20 shows a layer with a resistivity of about  $13.5 \Omega\text{m}$ , which points to a clay-silt layer when compared with the values in Table 1. This agrees well with the borehole data described by Aigner et al. (2024). The third layer with the resistivity of  $22 \Omega\text{m}$  and  $30 \Omega\text{m}$  respectively, could indicate a second aquifer, which was also detected by Aigner et al. (2024), who found that a second aquifer with

the resistivity value of  $30\Omega\text{m}$  at a depth below 35 m.

The model created through the data gathered with the  $6.25 \times 6.25\text{ m}$  loop, as seen in Figure 19, only shows the first two layers and is unable to resolve the third layer. The advantage of being able to resolve shallow layers with a smaller loop (**kirsch2006groundwater**), is counteracted by the effects of turn-off ramp as described by Aigner et al. (2021) and thus the need to discard the early time data. The results produced with the larger loop and the current of  $4.1\text{ A}$  seem to reproduce the results of earlier studies like Aigner et al. (2024) the best out of the configurations tested in this work.



**Fig. 18:** Optimised inversion of the sounding M028 of the first survey, which was measured with a  $12.5 \times 12.5$  m loop and 1.0 A of current. This sounding was done at the same location as M052 of the second survey. Subfigure (a) shows the comparison between modelled and measured impulse response as well as the measured error, (b) shows the comparison between modelled and measured apparent resistivities, (c) shows the final subsurface model of the resistivity, (d) shows the L-curve of this sounding with the chosen lambda value marked in orange.

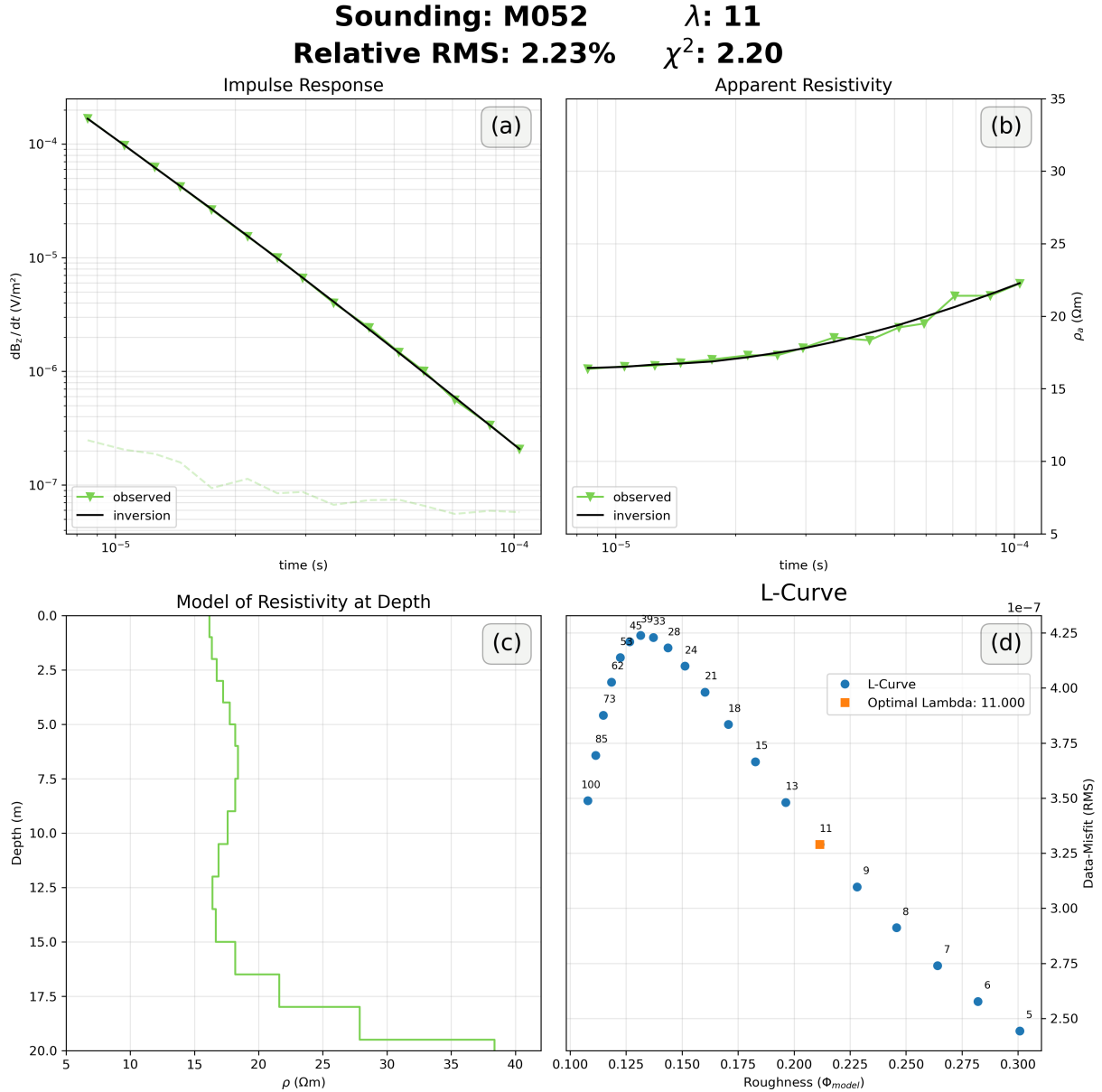


**Fig. 19:** Optimised inversion of the sounding M052 of the second survey, which was measured with a  $6.25 \times 6.25$  m loop and 4.1 A of current. This sounding was done at the same location as M028 of the first survey. Subfigure (a) shows the comparison between modelled and measured impulse response as well as the measured error, (b) shows the comparison between modelled and measured apparent resistivities, (c) shows the final subsurface model of the resistivity, (d) shows the L-curve of this sounding with the chosen lambda value marked in orange.

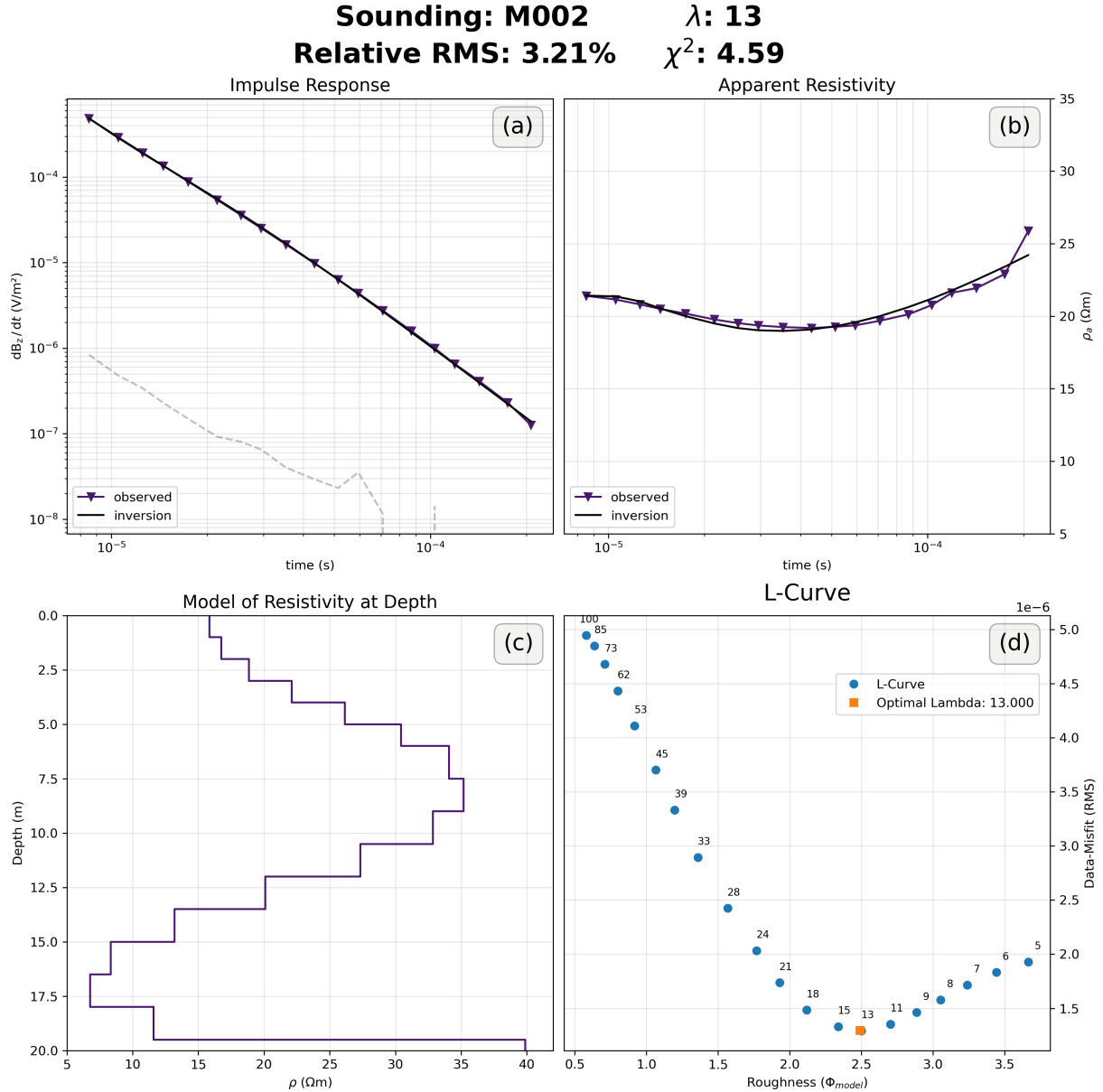


**Fig. 20:** Optimised inversion of the sounding M002 of the first survey, which was measured with a  $12.5 \times 12.5$  m loop and 4.1 A of current. Subfigure (a) shows the comparison between modelled and measured impulse response as well as the measured error, (b) shows the comparison between modelled and measured apparent resistivities, (c) shows the final subsurface model of the resistivity, (d) shows the L-curve of this sounding with the chosen lambda value marked in orange.

## 4 Conclusion

### List of Figures

1	Numerically modelled typical TEM response with the used subsurface model (a), the signal (b), and the apparent resistivity (c) . . . . .	2
2	Map of Sounding Locations in May . . . . .	9
3	Map of Sounding Locations in October . . . . .	9
4	Response Curves of the May Survey . . . . .	12
5	Anomalous Responses of the May Survey . . . . .	13
6	Response Curves of the October Survey . . . . .	14
7	Anomalous Responses of the October Survey . . . . .	15
8	Inversion With 10m Maximum Depth . . . . .	17
9	Inversion With 20m Maximum Depth . . . . .	17
10	Example of an ideal L-Curve . . . . .	19
11	Example of an usable L-Curve . . . . .	19
12	Example of an inverted L-Curve . . . . .	20
13	Example of a bad L-Curve . . . . .	20
14	Lambda Search Without Normalisation . . . . .	22
15	Lambda Search With Normalisation . . . . .	23
16	Example Lambda Search Working With Non-Ideal L-Curve . . . . .	23
17	Example Lambda Search Not Working . . . . .	24
18	Inversion of Sounding with the Large Loop and Small Current . . . . .	27
19	Inversion of Sounding with the Small Loop and Large Current . . . . .	28
20	Inversion of Sounding with the Large Loop and Large Current . . . . .	29

### List of Tables

1	Common Resistivity Values of Subsurface Materials . . . . .	6
2	Time Key Parameters of the TEM-FAST Device . . . . .	9
3	Device Settings in Both Surveys . . . . .	9
4	Summary of the search for an optimal Lambda . . . . .	22

### Declaration of competing interest

The authors declare that they have no known competing financial interests or personal relationships that could have appeared to influence the work reported in this thesis.

### Data availability

The python package for this thesis was developed in cooperation with Welkens (2025) and is building upon the routine from Aigner et al. (2021). It is available open-source and can be accessed on github ([https://github.com/pb-tuwien/Bsc\\_TEM\\_tools.git](https://github.com/pb-tuwien/Bsc_TEM_tools.git)). To facilitate full reproducibility of the results all data and python routines used throughout this work can also be accessed on github ([https://github.com/pb-tuwien/BSc\\_Soda\\_Lakes\\_Balogh.git](https://github.com/pb-tuwien/BSc_Soda_Lakes_Balogh.git))

### References

- Aigner, L., P. Högenauer, M. Bücker, and A. Flores Orozco (2021). “A Flexible Single Loop Setup for Water-Borne Transient Electromagnetic Sounding Applications”. In: *Sensors* 21.19, pp. 6624-. DOI: [10.3390/s21196624](https://doi.org/10.3390/s21196624).
- Aigner, L., H. Michel, T. Hermans, and A. F. Orozco (Aug. 1, 2025). “Stochastic Inversion of Transient Electromagnetic Data to Derive Aquifer Geometry and Associated Uncertainties”. In: *Geophysical Journal International* 242.2, ggaf236. DOI: [10.1093/gji/ggaf236](https://doi.org/10.1093/gji/ggaf236).
- Aigner, L., D. Werthmüller, and A. Flores Orozco (Apr. 1, 2024). “Sensitivity Analysis of Inverted Model Parameters from Transient Electromagnetic Measurements Affected by Induced Polarization Effects”. In: *Journal of Applied Geophysics* 223, p. 105334. DOI: [10.1016/j.jappgeo.2024.105334](https://doi.org/10.1016/j.jappgeo.2024.105334).
- Auken, E., N. Foged, J. J. Larsen, K. V. T. Lassen, P. K. Maurya, S. M. Dath, and T. T. Eiskjær (Jan. 2019). “tTEM — A Towed Transient Electromagnetic System for Detailed 3D Imaging of the Top 70 m of the Subsurface”. In: *GEOPHYSICS* 84.1, E13–E22. DOI: [10.1190/geo2018-0355.1](https://doi.org/10.1190/geo2018-0355.1).

- Auken, E., L. Pellerin, and K. I. Sørensen (2005). "Mutually Constrained Inversion (MCI) of Electrical and Electromagnetic Data". In: *SEG Technical Program Expanded Abstracts 2001*, pp. 1455–1458. DOI: 10.1190/1.1816378.
- Barsukov, P., E. Fainberg, and E. Khabensky (Jan. 1, 2006). "Chapter 3 Shallow Investigations by TEM-FAST Technique: Methodology and Examples". In: *Methods in Geochemistry and Geophysics*. Ed. by V. V. Spichak. Vol. 40. Elsevier, pp. 55–77. ISBN: 0076-6895. DOI: 10.1016/S0076-6895(06)40003-2.
- Boros, E. and L. Vörös (2025). "How Can Unique Alkaline Soda Waters Be Managed and Restored? Lake Neusiedl as the Largest Threatened European Example". In: *Ecohydrology* 18.2, e2738. DOI: 10.1002/eco.2738.
- Chandra, P. C. (2016). "The Time Domain Electromagnetic Method". In: *Groundwater Geophysics in Hard Rock*. United Kingdom: CRC Press, pp. 251–280. ISBN: 978-0-415-66463-9.
- Chengshuai, L., L. Han, Z. Zhanli, Z. Qingyang, D. Qianqian, Z. Teng, and Z. Mingxia (Nov. 2024). "Research on the Application of Transient Electromagnetic Exploration in Coal Mine Water Disaster Prevention and Control". In: *Journal of Physics: Conference Series* 2895.1, p. 012054. DOI: 10.1088/1742-6596/2895/1/012054.
- Christiansen, A. V., E. Auken, and K. Sørensen (2006). "The Transient Electromagnetic Method". In: *Groundwater Geophysics: A Tool for Hydrogeology*. Ed. by R. Kirsch. Berlin, Heidelberg: Springer Berlin Heidelberg, pp. 179–225. ISBN: 978-3-540-29387-3. DOI: 10.1007/3-540-29387-6\_6.
- Culturera, A. and L. Callegaro (Aug. 2020). "A Simple Algorithm to Find the L-curve Corner in the Regularisation of Ill-Posed Inverse Problems". In: *IOP SciNotes* 1.2, p. 025004. DOI: 10.1088/2633-1357/abad0d.
- Danielsen, J. E., E. Auken, F. Jørgensen, V. Søndergaard, and K. I. Sørensen (Oct. 1, 2003). "The Application of the Transient Electromagnetic Method in Hydrogeophysical Surveys". In: *Journal of Applied Geophysics*. Geophysical Investigations of Buried Quaternary Valleys in the Formerly Glaciated NW European Lowland: Significance for Groundwater Exploration 53.4, pp. 181–198. DOI: 10.1016/j.jappgeo.2003.08.004.
- Everett, M. E. (2013). "Electromagnetic Induction". In: *Near-Surface Applied Geophysics*. United States: Cambridge University Press, pp. 200–238. ISBN: 978-1-107-01877-8.
- Farquharson, C. G. and D. W. Oldenburg (2004). "A Comparison of Automatic Techniques for Estimating the Regularization Parameter in Non-Linear Inverse Problems". In: *Geophysical Journal International* 156.3, pp. 411–425. DOI: 10.1111/j.1365-246X.2004.02190.x.
- Fitterman, D. V. and M. T. Stewart (1986). "Transient Electromagnetic Sounding for Groundwater". In: *Geophysics* 51.4, pp. 995–1005. DOI: 10.1190/1.1442158.
- Galazoulas, E. C., Y. C. Mertzanides, C. P. Petalas, and E. K. Kargiotis (Mar. 1, 2015). "Large Scale Electrical Resistivity Tomography Survey Correlated to Hydrogeological Data for Mapping Groundwater Salinization: A Case Study from a Multilayered Coastal Aquifer in Rhodope, Northeastern Greece". In: *Environmental Processes* 2.1, pp. 19–35. DOI: 10.1007/s40710-015-0061-y.
- George, N. J., A. M. Ekanem, J. E. Thomas, and T. A. Harry (Mar. 1, 2022). "Modelling the Effect of Geo-Matrix Conduction on the Bulk and Pore Water Resistivity in Hydrogeological Sedimentary Beddings". In: *Modeling Earth Systems and Environment* 8.1, pp. 1335–1349. DOI: 10.1007/s40808-021-01161-0.
- Gómez, E., M. Larsson, T. Dahlin, G. Barmen, and J.-E. Rosberg (Jan. 28, 2019). "Alluvial Aquifer Thickness and Bedrock Structure Delineation by Electromagnetic Methods in the Highlands of Bolivia". In: *Environmental Earth Sciences* 78.3, p. 84. DOI: 10.1007/s12665-019-8074-x.
- Gonzales Amaya, A., J. Mårdh, and T. Dahlin (Jan. 19, 2018). "Delimiting a Saline Water Zone in Quaternary Fluvial–Alluvial Deposits Using Transient Electromagnetic: A Case Study in Punata, Bolivia". In: *Environmental Earth Sciences* 77.2, p. 46. DOI: 10.1007/s12665-017-7213-5.
- Hansen, P. C. (1992). "Analysis of Discrete Ill-Posed Problems by Means of the L-Curve".

- In: *SIAM review* 34.4, pp. 561–580. DOI: 10.1137/1034115.
- Kirsch, R. (2006). “Petrophysical Properties of Permeable and Low-Permeable Rocks”. In: *Groundwater Geophysics: A Tool for Hydrogeology*. Ed. by R. Kirsch. Berlin, Heidelberg: Springer Berlin Heidelberg, pp. 1–22. ISBN: 978-3-540-29387-3.
- Lloyd, J. J., C. J. Taylor, R. S. Lawson, and R. A. Shields (Oct. 1, 1997). “The Use of the L-curve Method in the Inversion of Diffusion Battery Data”. In: *Journal of Aerosol Science* 28.7, pp. 1251–1264. DOI: 10.1016/S0021-8502(97)00018-9.
- Obukhov, G. G. (1968). “The Fields of a Horizontal Electric Dipole Over an Uneven Insulating Basement”. In: *Exploration Geophysics* 50, p. 100.
- Rücker, C., T. Günther, and F. M. Wagner (Dec. 1, 2017). “pyGIMLi: An Open-Source Library for Modelling and Inversion in Geophysics”. In: *Computers & Geosciences* 109, pp. 106–123. DOI: 10.1016/j.cageo.2017.07.011.
- Siemon, B. (2009). “Electromagnetic Methods – Frequency Domain”. In: *Groundwater Geophysics: A Tool for Hydrogeology*. Ed. by R. Kirsch. Berlin, Heidelberg: Springer Berlin Heidelberg, pp. 155–178. ISBN: 978-3-540-88405-7. DOI: 10.1007/978-3-540-88405-7\_5.
- Sorensen, K. I. and E. Auken (Sept. 1, 2004). “SkyTEM—a New High-resolution Helicopter Transient Electromagnetic System”. In: *Exploration Geophysics* 35.3, pp. 194–202. DOI: 10.1071/EG04194.
- Su, M., M. Chu, Y. Xue, X. Ma, and Z. Ju (June 1, 2024). “Response Analysis and Application of the TEM Using Small-Fixed Loops”. In: *Acta Geotechnica* 19.6, pp. 3537–3553. DOI: 10.1007/s11440-023-02103-z.
- Welkens, J. (2025). “Comparison of Subsurface Geophysical Models of Hutweidenlacke (Nationalpark Seewinkel) Based on the Transient Electromagnetic Method”. Bachelor’s Thesis, unpublished. Vienna, Austria: Research Unit Geophysics, Department of Geodesy and Geoinformation, TU Wien.
- Werthmüller, D. (Nov. 2017). “An Open-Source Full 3D Electromagnetic Modeler for 1D VTI Media in Python: Empymod”. In: *GEO-* PHYSICS 82.6, WB9–WB19. DOI: 10.1190/geo2016-0626.1.
- Xue, G., H. Li, Y. He, J. Xue, and X. Wu (2020). “Development of the Inversion Method for Transient Electromagnetic Data”. In: *IEEE Access* 8, pp. 146172–146181. DOI: 10.1109/ACCESS.2020.3013626.
- Zhdanov, M. S. (2002). *Geophysical Inverse Theory and Regularization Problems*. 1st ed. Methods in Geochemistry and Geophysics. Amsterdam: Elsevier. ISBN: 978-0-444-51089-1.
- Zhou, Y., P. Jianwei, L. Hao, W. Zhongmei, Z. Jiang, L. Haixin, and L. Jiaxu (Nov. 10, 2022). “Multi-Turn Small-Loop Transient Electromagnetic Data Processing Using Constraints from Borehole and Electrical Resistivity Tomography Data”. In: *Arabian Journal of Geosciences* 15.22, p. 1675. DOI: 10.1007/s12517-022-10952-3.